Particulate and dissolved fluorescent organic matter fractionation and composition: Abiotic and ecological controls in the Southern Ocean

Miguel Cabrera-Brufau, Cèlia Marrasé, Eva Ortega-Retuerta, Sdena Nunes, Marta Estrada, M Montserrat Sala, Dolors Vaqué, Gonzalo L Pérez, Rafel Simó, Pedro Cermeño

Science of the Total Environment 844 (2022) 156921

Contents lists available at ScienceDirect

Science of the Total Environment

journal homepage: www.elsevier.com/locate/scitotenv

Particulate and dissolved fluorescent organic matter fractionation and composition: Abiotic and ecological controls in the Southern Ocean

Miguel Cabrera-Brufau [a,b], Cèlia Marrasé [a,*], Eva Ortega-Retuerta [c], Sdena Nunes [d], Marta Estrada [a], M. Montserrat Sala [a], Dolors Vaqué [a], Gonzalo L. Pérez [e], Rafel Simó [a], Pedro Cermeño [a]

[a] Department of Marine Biology and Oceanography, Institute of Marine Sciences (CSIC), Barcelona, Spain
[b] Department of Evolutionary Biology, Ecology and Environmental Sciences, University of Barcelona, Barcelona, Spain
[c] CNRS/Sorbonne Université, UMR7621 Laboratoire d'Océanographie Microbienne, Banyuls sur Mer, France
[d] Red Sea Research Center, King Abdullah University of Science and Technology (KAUST), Thuwal, Saudi Arabia
[e] GESAP, INBIOMA (UNComahue-CONICET), San Carlos de Bariloche, Argentina

HIGHLIGHTS

- Fluorescent Organic Matter (FOM) was measured in filtered and unfiltered seawater.
- Protein-like FOM was mostly in particulate form and visible FOM in dissolved form.
- Non-diatom Chl *a* accounted for 91 % of particulate protein-like FOM variability.
- Protein-like FOM fractionation was related to signals of viral infection and grazing.
- Visible FOM composition was affected by photobleaching and biotic modification.

GRAPHICAL ABSTRACT

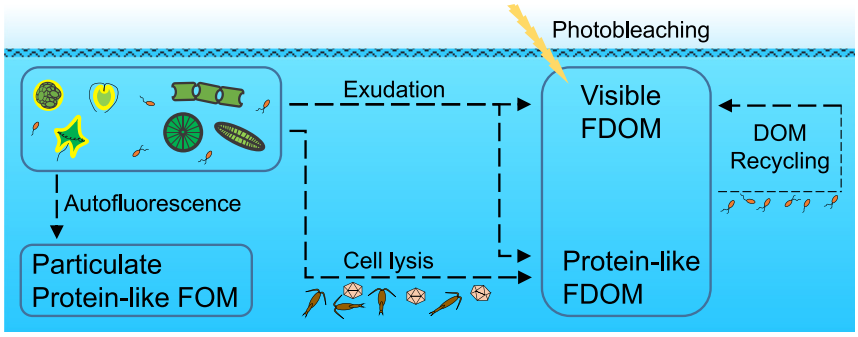

ARTICLE INFO

Editor: Damia Barcelo

Keywords:
Fluorescent organic matter
Phytoplankton
Bloom dynamics
OM fractionation
Photobleaching
Southern Ocean

ABSTRACT

Phytoplankton-derived organic matter sustains heterotrophic marine life in regions away from terrestrial inputs such as the Southern Ocean. Fluorescence spectroscopy has long been used to characterize the fluorescent organic matter (FOM) pool. However, most studies focus only in the dissolved FOM fraction (FDOM) disregarding the contribution of particles. In order to assess the dynamics and drivers of the dissolved and particulate fractions of FOM, we used a Lagrangian approach to follow the time evolution of phytoplankton proliferations at four different sites in the Southern Ocean and compared the FOM in filtered and unfiltered seawater aliquots. We found that filtration had little effects on FOM visible spectrum fluorescence intensities, implying that most of this signal was due to dissolved fluorophores. On the other hand, protein-like fluorescence was strongly supressed by filtration, with fluorescence of particles accounting for up to 90 % of the total protein-like FOM. Photobleaching was identified as the main driver of visible FDOM composition, which was better described by indices of phytoplankton photoacclimation than by measurements of the incident solar radiation dose. In contrast, protein-like FOM intensity and fractionation were primarily related to abundance, composition and physiological state of phytoplankton proliferations. The chlorophyll *a* concentration from non-diatom phytoplankton explained 91 % of the particulate protein-like FOM variability. The proportion of protein-like fluorescence found in the dissolved phase was predicted by the combination of potential viral and grazing pressures, which accounted for 51 and 29 % of its variability, respectively. Our results show that comparing FOM measurements from filtered and unfiltered seawater provides relevant information on the taxonomic composition and cell integrity of phytoplankton communities. A better understanding of the commonly overlooked FOM fractionation

* Corresponding author at: Dep. of Marine Biology and Oceanography, Institut de Ciències del Mar (ICM-CSIC), Passeig Marítim de la Barceloneta, 37-49, 08003 Barcelona, Spain.
E-mail address: celia@icm.csic.es (C. Marrasé).

http://dx.doi.org/10.1016/j.scitotenv.2022.156921
Received 9 April 2022; Received in revised form 3 June 2022; Accepted 20 June 2022
Available online 24 June 2022

process is essential for the implementation of in situ fluorescence sensors and will also help us better understand the processes that govern OM cycling in marine systems.

1. Introduction

Phytoplankton are the main producers of organic matter (OM) in the ocean, being responsible for approximately half of the annual global net primary production (Field et al., 1998). These organisms produce particulate organic matter (POM) as part of their cells biomass and, additionally, exude dissolved organic matter (DOM) (Marañón et al., 2004). The composition of phytoplankton-derived OM is of utmost importance for marine ecosystems, as it constitutes the energy basis and carbon source for most heterotrophic life in the ocean. Among the OM characterization techniques in oceanography, fluorescence spectroscopy uses the naturally fluorescent fraction of organic matter to broadly characterize its composition (Coble, 2007). This technique is highly widespread, as it represents a fast and inexpensive method to gain insight into OM composition and can be easily integrated in autonomous monitoring devices such as ARGO floats and gliders (Moore et al., 2009; Carstea et al., 2020).

Two main categories of fluorescent organic matter (FOM) substances can be distinguished: humic-like FOM, composed of highly condensed, C-rich aromatic substances that fluoresce in the visible spectrum, and protein-like FOM, with fluorescent signals in the ultraviolet spectrum similar to those of the aromatic amino acids tryptophan and tyrosine (Yamashita and Tanoue, 2003; Coble, 2007; Martínez-Pérez et al., 2017). These two fractions of fluorescent organic matter have been extensively studied and their sources and sinks in marine systems are relatively well identified (Nelson and Gauglitz, 2016). In the open ocean, away from terrestrial inputs, surface humic-like FOM composition is mainly controlled by solar radiation, which supresses its visible fluorescence in a process known as photobleaching (Dainard et al., 2015; Mopper et al., 2015). Marine organisms also modify visible FOM composition through the production of humic-like substances by phytoplankton (Romera-Castillo et al., 2010; Fukuzaki et al., 2014) and the production and consumption of a variety of humic-like substances by heterotrophic prokaryotes (Romera-Castillo et al., 2011). Protein-like fluorescence distribution in the ocean is mainly linked to biotic processes of OM production and consumption (Jørgensen et al., 2011; Lønborg et al., 2015) and it represents an attractive substrate for prokaryotes (Lønborg et al., 2010), probably due to a high content in nitrogen, a limiting nutrient in marine systems (Elser et al., 2007). Suspended biotic particles, such as phytoplankton and bacteria, emit protein-like fluorescence (Determann et al., 1998) and contain base-extractable materials with fluorescence properties similar to those of natural FOM (Brym et al., 2014; Kinsey et al., 2018). Yet, most studies using fluorescence to characterize OM composition focus solely on the dissolved FOM pool (FDOM), disregarding the role of particles excluded by filtration (e.g. Murphy et al., 2008; Para et al., 2010; Cao et al., 2020). This common approach overlooks the potentially important contribution of biotic particles to OM fluorescence, which might lead to misinterpretation of "FDOM" distributions obtained from online sensors measuring in situ, non-filtered seawater fluorescence. We hypothesize that overseeing the particulate FOM might have prevented us from identifying ecologically relevant processes associated with particle fragmentation.

The partitioning of organic matter between the particulate (POM) and dissolved (DOM) pools has important biogeochemical and ecological implications, as these size-fractions are subject to contrasting transport and biological consumption processes in the ocean (Zhang et al., 2018). Phytoplankton-derived POM can sink on its own, and also comprises the basis for the classical food web supporting fish and other marine metazoans (Legendre, 1990; Fortier et al., 1994). Phytoplankton-derived DOM, by contrast, requires vertical mixing and water mass downwelling to be exported to depth, and is mostly recycled, re-entered into the food web and remineralized by heterotrophic prokaryotes in the surface ocean through the microbial loop (Azam et al., 1983). Thus, understanding the processes that control OM fractionation is essential to predict the fate of phytoplankton biomass and its channelling either through the classical food web or the microbial loop. In this context, collapse of phytoplankton blooms and solubilization of their POM via grazer-mediated fragmentation or viral lysis have a substantial impact on OM cycling and constitute important sources of DOM in productive ocean regions (Carlson and Hansell, 2015). However, studying in situ these biotic processes of phytoplanktonic OM fragmentation and their impact on FOM composition is challenging, as it requires intensive sampling strategies to accurately describe their dynamics.

The Southern Ocean is one of the most productive marine regions globally and is characterized by an extreme seasonality. During the Antarctic productive season, as the day lengthens and sea-ice recedes, phytoplankton blooms develop and collapse under intense UV irradiances (Sullivan et al., 1993; Landry et al., 2002; Mendes et al., 2012; Taylor et al., 2013; Costa et al., 2020), requiring phytoplankton to implement photoacclimation strategies to cope with photo-oxidative stress (Kropuenske et al., 2009; Alderkamp et al., 2013). These conditions make the Antarctic waters of the Southern Ocean an ideal setting to study the effects of the development of marine plankton communities and intense solar radiation over the FOM composition. Multiple studies have described the distribution and potential drivers of organic matter composition in the Southern Ocean. Photobleaching and biological production and consumption have been proposed as important controls of FOM composition in Antarctic waters (e.g. Misic et al., 2006; D'Sa and Kim, 2017; Chen et al., 2019; D'Sa et al., 2021). However, most studies lack a detailed biological characterization (often using chlorophyll *a* concentration as the only biological parameter) and do not report measurements of solar radiation. In addition, although some surveys have reported fluorescence of unfiltered samples (Wedborg et al., 2007), most have focused solely on FDOM distributions and, to our knowledge, no work to date has investigated the fractionation of FOM into its dissolved and particulate pools in Antarctic waters.

In this study, we investigate the dynamics and drivers of the particulate and dissolved fractions of FOM from four Antarctic phytoplankton proliferations, which were tracked using a Lagrangian approach during the summer of 2015 (Nunes et al., 2019). In particular, we (i) use combined measurements of solar irradiance and phytoplankton photoacclimation to evaluate the effects of photobleaching over FOM composition and (ii) relate the dynamics and fractionation of the particulate and dissolved FOM pools with the biological composition and state of plankton proliferations.

2. Material and methods

2.1. Sampling strategy

Four Southern Ocean sites, north of South Orkney Islands (NSO), southeast of South Orkney Islands (SSO), northwest of South Georgia Island (NSG) and west of Anvers Island (WA), were sampled sequentially from January 10th 2015 to February 3rd 2015 using a lagrangian approach in each (Supplementary Fig. 1). With the aim of following the same water mass, standard WOCE (World Ocean Circulation Experiment) lagrangian drifters were used in NSO, NSG and WA sites, whereas the positioning of samplings at SSO was determined by tracking the movement of reference icebergs. Water samples were obtained from surface (4 m) to 200 m depth at least once a day at ~8:30 local time. Sampling was carried out by means of CTD casts attached to a rosette of 12-L Niskin PVC bottles. In addition, one high frequency (every 4 h) sampling, covering at least a 32-h cycle, was conducted in each site. The main hydrographic fronts were located with reference to continuous temperature and salinity records and Doppler-derived current velocities. Further details on the sampling strategy and hydrographic conditions encountered during the survey can

be found in Nunes et al. (2019). Data from a total of 53 stations is presented (16 from NSO, 15 from SSO, 13 from NSG and 9 from WA site).

2.2. Environmental parameters

Temperature and salinity profiles were obtained with a CTD probe (SBE911 plus) attached to the sampling rosette. Estimations of mixed layer depth were performed based on the CTD profiles following Levitus (1982). Samples for inorganic nutrient determination (10 ml) were collected and stored at −20 °C until analysis. At the home laboratory, concentrations of nitrate (NO_3^-), phosphate (PO_4^{3-}) and silicate (SiO_4^{2-}) were determined with an auto-analyzer (Bran Luebbe AA3), using common spectrophotometric measurements (Grasshoff et al., 1978). As described in Zamanillo et al. (2019), average diffuse attenuation coefficients in the euphotic zone (K_d) were determined for the photosynthetically active radiation (PAR) broadband (400–700 nm) as the slope of linear regressions between logarithmic irradiances and depth. The daily-average solar radiation dose in the mixed layer (SRD) was then calculated based on the estimated mixed layer depths, the obtained PAR attenuation coefficients (K_d) and daily irradiances (Vallina and Simó, 2007):

$$SRD = \frac{I}{K_d * MLD} * \left(1 - e^{-K_d * MLD}\right)$$

where, I is the global surface radiation intensity (W m^{-2}) averaged across the 24 h previous to sampling, K_d is the average diffuse attenuation coefficient of PAR (m^{-1}) and MLD is the mixed layer depth (m). The above parameters used for SRD calculation are reported in the supplementary materials as averages for each site visited (Supplementary Table 1).

2.3. Organic carbon and nitrogen

For the determination of particulate organic carbon (POC) and nitrogen (PON), 1000 ml of seawater were filtered through precombusted glass fiber filters (GF/F, Whatman) and stored frozen (−20 °C) until analysis. Carbon and nitrogen content in the filters was determined with an elemental analyzer (Perkin-Elmer 2400 CHN). Samples for total organic carbon (TOC) quantification were collected in 30 ml acid-cleaned polycarbonate bottles and stored at −20 °C until analysis at home laboratory. C content was determined after inorganic C removal through acidification using a Shimadzu TOC VCSH instrument, calibrated with potassium hydrogen phthalate and using MQ water as blank and deep Sargasso Sea water as the reference (Batch-13 Lot//08-13, measured TOC: 40.19 ± 1.3 μM, Hansell Laboratory. University of Miami, RSMAS).

2.4. Fluorescent organic matter characterization

Samples for FOM characterization were collected directly from the CTD Niskin bottles into acid-cleaned 250 ml glass bottles rinsed three times with sample before filling. The cuvettes and glass filtration system were stored in a bath of hydrochloric acid (1 %) between stations and thoroughly rinsed with MQ water before their use. An aliquot of each sample was filtered through 0.2 μm pore-size polycarbonate filters previously rinsed with abundant MQ water in a glass filtration system under low positive pressure applied with ultrapure N_2 gas. For both filtered and unfiltered aliquots, fluorescence was recorded using a Perkin Elmer LS55 spectrofluorometer with 1 cm quartz cuvettes. Absorbance spectra (250–750 nm) were collected using a Perkin Elmer Lambda 850 spectrophotometer with 10 cm path-length quartz cells and transformed into absorption coefficients multiplying the absorbances by 2.303/L, where L is the cuvette path length in meters.

Fluorescence was measured using a custom program within the fluorometer FL-Winlab software. This measuring program was designed to measure a sequence of 5 pairs of pre-selected excitation/emission wavelengths 4 consecutive times. The excitation and emission slit widths were set to 10 nm and the whole duration of the measuring program was 82 s. The 5 excitation/emission pairs (hereinafter peaks) were selected based on the most common features typically observed in marine samples. Four peaks were selected following Coble (1996): peak A (ex/em 250/435 nm), originally described as indicative of general humic substances; peak M (ex/em 320/410 nm), described as marine humic substances and reported to be of phytoplanktonic origin (Romera-Castillo et al., 2010); peak C (ex/em 340/440 nm), characteristic of terrestrial inputs and microbial byproducts (Romera-Castillo et al., 2011); and peak T (ex/em 280/350 nm), indicative of protein-like substances, such as dissolved tryptophan (Yamashita and Tanoue, 2003) and found to be highly bioavailable (Lønborg et al., 2010). An additional peak was selected at ex/em 370/460 nm named peak F (Kraus et al., 2010), which is commonly used in commercially available on-line sensors (Carstea et al., 2020). The location of this peak F is in the upper-wavelength limits of the peak C region and is similar to fluorescence maxima of components C2 reported in Yamashita et al. (2011) and SQ2 reported in Cory and McKnight (2005) with presumed terrestrial and microbial origins, respectively.

The above measuring program was used to record the fluorescence of unfiltered and filtered aliquots of each sample, rinsing the cuvette 3 times with the corresponding aliquot before filling it. In order to ensure homogeneous distribution of particles, unfiltered aliquots were shaken gently by hand before filling the cuvette. For each aliquot, the same measuring program was run 1 to 3 times, depending on the deviation observed between the 4 consecutive measurements of each peak, rinsing (with 1 % HCl and 3xMQ) and re-filling the cuvette each time. This approach yielded very consistent fluorescent intensities, with a mean relative standard error of 1.8 ± 0.9 % across all samples and peaks, and with no appreciable trend between the 4 consecutive measurements of each program run, thus discarding any influence of particle sedimentation in the fluorescence signal during the 82 s of each run. Fluorescence of blanks was recorded with the same program using MQ water produced on-board. The daily fluorescence values obtained from unfiltered MQ and 0.2 μm-filtered MQ were subtracted from those of unfiltered and filtered aliquots, respectively. Mean blank fluorescence intensities for each peak are reported in Supplementary Table 2. All fluorescence data is reported in 10^{-3} Raman Units (RU) after normalization to the integrated area of the Raman scatter peak (ex: 350 nm, em: 371–428 nm) measured daily in MQ blanks (Lawaetz and Stedmon, 2009). Despite the low absorption values obtained for unfiltered and filtered aliquots (absorption coefficients <1.6 m^{-1}, Supplementary Fig. 2), correction of inner-filter effects was applied to all fluorescence data following Kothawala et al. (2013) to avoid propagation of error when computing derived fluorescence parameters.

Throughout this work, we report the fluorescence of peaks A, M, C, and F in filtered and unfiltered aliquots and, given that these peaks are located in the visible emission region usually influenced by overlapping of fulvic and humic components, hereinafter we refer to them collectively as visible-fluorescence peaks following Stedmon and Nelson (2015). For protein-like fluorescence (Peak T), we define peak Td as the fluorescence of filtered aliquots and, additionally, we calculate (i) the apparent peak T particulate fluorescence (peak Tp) of each sample as the difference in fluorescence between unfiltered and filtered aliquots, and (ii) the proportion of dissolved peak T (%Tdiss) as the ratio between the fluorescence of filtered and unfiltered aliquots.

2.5. Microbiological variables

Samples for determination of the heterotrophic prokaryote abundance (HPA) were fixed with paraformaldehyde (1 %) and glutaraldehyde (0.05 %), and stored at −80 °C until analysis through flow cytometry. The quantification was performed with a FACSCalibur flow cytometer after staining with SYBR-Green I following Gasol and Del Giorgio (2000). Samples for viral abundance determination were fixed with glutaraldehyde (0.5 % final concentration) and kept frozen at −80 °C until analysis by flow cytometry. Viral subpopulations were discriminated in bivariate scatter plots of side scatter versus green fluorescence of stained nucleic acids (with SYBR Green I) as described in Evans et al. (2009). The viral

subpopulations were grouped according to their fluorescence signal and presumed hosts (Evans et al., 2009; Sotomayor-Garcia et al., 2020); high fluorescence viral abundance (HFVA) refers to viral subpopulation V3 and is presumed to be mainly composed of viruses of eukaryotes, whereas the low fluorescence viral abundance (LFVA) consisted on viral subpopulations V1 and V2, considered to be mainly bacteriophages (Brussaard et al., 2010).

2.6. Phytoplanktonic parameters

For the determination of chlorophyll *a* (Chl *a*) concentration, 100 ml of seawater were filtered through 25 mm diameter Whatman GF/F filters. Filters were stored at −20 °C for several hours prior to their analysis on board. Extraction was performed in acetone (90 %) at 4 °C for 24 h. Fluorescence of extracts was measured, following Yentsch and Menzel (1963), with a calibrated Turner Designs fluorometer (model 10-AU-005 field fluorometer) equipped with an excitation filter letting through the 340–500 nm wavelength range and an emission filter letting through wavelengths above 665 nm. As described in Nunes et al. (2019), high performance liquid chromatography was used to determine phytoplankton pigment composition following the method of Latasa (2014). Contribution of microalgal groups to total Chl *a* was calculated using CHEMTAX software (version 1.95) from the composition of 11 from the 32 pigments identified. Seven pigmentary phytoplankton groups were quantified: chlorophytes, cryptophytes, diatoms, dinoflagellates, haptophytes, prasinophytes and pelagophytes. Two pigmentary indices were also derived from the pigment composition as described in Nunes et al. (2019), related to herbivory pressure and light stress. As pigment composition can be altered by variations in irradiance (Higgins et al., 2011), a photoprotective pigment index was computed to assess the degree of light stress of the phytoplankton populations encountered. This index was calculated as the ratio of diadinoxanthin (Ddx), the main photoprotective pigment of various phytoplankton groups, to the sum of the main light harvesting carotenoids (LHC): fucoxanthin, 19′-butanoyloxyfucoxanthin, 19′-hexanoyloxyfucoxanthin (19-Hex) and peridinin. This photoprotective index (Ddx:LHC) and other similar indices, based on relative abundance of photoprotective to light harvesting pigments, have been shown to increase in phytoplankton populations under high irradiation stress (Moline, 1998; Cheah et al., 2017; Nunes et al., 2019). The pigmentary herbivory index (Herbiv) was calculated as the ratio of the sum of phaeophorbides and phaeophytines (Chl *a* degradation products) to Chl *a* concentration, following Mendes et al. (2015). Phytoplankton abundance and taxonomic composition were also analyzed through optical microscopy as described in Nunes et al. (2019). Briefly, samples were fixed with formalin-hexamine (1 % final concentration) and stored in the dark. For analysis, an aliquot (100 ml) was sedimented (48 h) and phytoplankton was identified and quantified with an inverted microscope (Utermöhl, 1958) to the lowest taxonomical level possible. Biovolumes were estimated based on mean length and width of each taxon identified, assuming different simplified geometric shapes (Hillebrand et al., 1999). Setae and other appendages were excluded from the biovolume estimation.

2.7. Statistical analyses

All statistical analyses and plots presented were done in R (4.1.2), using packages *tidyverse*, *broom*, *FactoMineR*, *ggplot2* and *ggpubr*. Temporal trends were identified as significant ($p < 0.05$) correlations (Pearson's R) between the examined parameter and the time elapsed since the first sampling at each location. The selection of variables for the principal component analysis was done using least square regressions to determine the main predictors of the FOM composition parameters examined: FDOM peaks A, C, M, F and Td; the apparent particulate fluorescence of peak Tp, the C:M peak ratio and the proportion of peak T found in the dissolved phase (%Tdiss). We used the coefficient of determination (R^2) yielded from linear regressions of the log-transformed data as the criteria of inclusion: Only the top 5 variables with the highest coefficient of determination for each FOM parameter were used for the principal component analysis. Despite their high explanatory power, primary production and prokaryotic heterotrophic production rates were excluded due to their small number of observations. This selection yielded 11 variables and 2 ratios, most of them shared among FOM parameters, as the ones with highest explanatory power. We used the squared cosines (cos^2) to evaluate the quality of representation of a given variable in the PCA analysis (Abdi and Williams, 2010). For the evaluation of the relative apparent photosensitivity gradient between visible-fluorescence peaks A, M, C and F presented in Section 3.4.1, the fluorescence of each peak was normalized by dividing all fluorescence intensities of surface samples by the maximum fluorescence observed among them for each peak. F-test was used to compare the fitness of regression models with increasing complexity (i.e. with different number of predictors) and to compute the variance explained by each predictor. Comparison of means was performed with Student or Welch *t*-tests, depending on the results yielded by the test for equality of variances between the two groups.

3. Results & discussion

3.1. General site characterization

The four sites visited were characterized by distinct environmental and biological conditions (Table 1), which have been described extensively in previous works (Nunes et al., 2019; Zamanillo et al., 2019; Sotomayor-Garcia et al., 2020). NSG presented the warmest sea surface temperature (SST), reaching 5.1 °C, while WA had colder waters (1.4 ± 0.1 °C). Despite their proximity, NSO and SSO exhibited marked differences in SST and sea surface salinity (SSS). NSO appeared to be warming, probably due to an increasing solar radiation dose (SRD). SSO presented the coldest waters (−0.75 ± 0.11 °C) and the lowest salinity of all sites, indicative of melting of sea-ice, which had reduced its cover from >50 % in the previous month to >25 % by the time of sampling (Zamanillo et al., 2019). The four sites presented parallel ordinations by SRD and phytoplankton photoprotective index (Ddx:LHC): highest values at SSO, then NSO, WA, and lowest at NSG. Regarding phytoplankton biomass and community structure (Nunes et al., 2019), the highest Chl *a* concentrations were found at NSG, with a taxonomic composition dominated by diatoms. WA had the second highest Chl *a* value, with a phytoplankton assemblage composed mainly of cryptophytes. This group was also the dominant in NSO, albeit with significant contributions of haptophytes and diatoms and a lower overall Chl *a* concentration. SSO presented the lowest Chl *a* concentrations, with haptophytes as the dominant phytoplankton group.

The phytoplankton assemblages at the four sites were in different stages of bloom development, as revealed by the abundances of heterotrophic prokaryotes and by the values and temporal trends of other biotic parameters (Table 1). NSO was at an early stage of the seasonal bloom, with stable Chl *a* values even when the grazing pressure increased throughout the sampling interval, as derived from the pigmentary herbivory index (Herbiv). SSO was at an even earlier stage of development due to recent sea-ice melt, indicated by low salinity, temperature and Chl *a* concentration, as well a high proportion of ice-associated diatoms such as *Fragilariopsis* spp. (Cefarelli et al., 2011; Nunes et al., 2019). Additionally, sea-ice influence was probably responsible for the high HPA:Chl *a* ratio observed at SSO, as organic materials released from sea-ice, such as transparent exopolymers (Zamanillo et al., 2019), would have relieved prokaryotic activity from its dependence on phytoplanktonic OM. This presumed input of sea-ice OM in SSO is also corroborated by the high relative concentrations of POC and TOC with respect to Chl *a* (Supplementary Fig. 3) as well as by the high abundance of ciliates, which are active consumers of prokaryotes (Supplementary Table 3).

By contrast, the WA and NSG sites exhibited features of being in an advanced stage of bloom development (Nunes et al., 2019), with relatively high concentrations of Chl *a* at the beginning but decreasing markedly throughout the visit (Table 1). NSG was characterized by the highest herbivory pressure (Herbiv) and HPA values, which increased significantly during the sampling interval (Table 1), indicative of grazer-induced

Table 1
Mean ± standard deviation and temporal trend of surface samples during the visit of each site. Significant temporal trends are shown below each mean as Pearson correlation coefficient of each variable with the time elapsed since the first sampling of each site, significance codes are * ($p < 0.05$), ** ($p < 0.01$) and *** ($p < 0.001$). SST: sea surface temperature. SSS: sea surface salinity. SRD: solar radiation dose. Ddx: LHC: photoprotective pigment index (see methods). HPA: heterotrophic prokaryotes abundance. HFVA: high fluorescence viral abundance. LFVA: low fluorescence viral abundance.

	NSO	SSO	NSG	WA
Date of arrival	1/10/2015	1/16/2015	1/23/2015	2/2/2015
Duration of visit	118 h	104 h	72 h	32 h
SST (°C)	0.59 ± 0.15	−0.75 ± 0.11	4.77 ± 0.47	1.46 ± 0.09
	*0.63**			
SSS (psu)	33.83 ± 0.08	33.15 ± 0.05	33.74 ± 0.02	33.41 ± 0.03
	*−0.78***			*0.84***
SRD (W m^{-2})	73.18 ± 30.46	101.73 ± 20.28	22.75 ± 7.30	47.05 ± 10.65
	*0.62**			
Nitrate (μM)	27.3 ± 1.9	27.5 ± 3.2	16.9 ± 1.4	18.7 ± 0.9
Phosphate (μM)	1.99 ± 0.21	2.14 ± 0.25	1.28 ± 0.15	1.79 ± 0.16
			*0.74***	*0.73**
Silicate (μM)	47.9 ± 4.1	47.3 ± 4.7	2.0 ± 0.4	49.7 ± 3.7
Chl *a* (μg L^{-1})	1.89 ± 0.24	0.32 ± 0.06	4.32 ± 2.10	4.14 ± 0.45
			*−0.78***	*−0.69**
Ddx:LHC	0.35 ± 0.06	0.60 ± 0.06	0.20 ± 0.04	0.25 ± 0.04
Herbiv	0.15 ± 0.04	0.19 ± 0.09	0.21 ± 0.08	0.09 ± 0.01
	*0.74***	*−0.56**	*0.95****	
Dominant phytoplankton CHEMTAX group	Cryptophytes	Haptophytes	Diatoms	Cryptophytes
HPA (cell $ml^{-1} \times 10^5$)	2.34 ± 0.46	2.67 ± 0.32	5.45 ± 0.85	3.39 ± 0.93
			*0.85****	
HFVA (virus $ml^{-1} \times 10^5$)	2.8 ± 0.9	1.6 ± 0.5	21.4 ± 12.1	8.9 ± 5.1
				*0.70**
LFVA (virus $ml^{-1} \times 10^6$)	4.2 ± 2.0	4.1 ± 4.8	19.3 ± 9.7	13.1 ± 4.4
HPA:Chl *a* (10^5 cell ng^{-1})	1.25 ± 0.26	8.64 ± 1.50	1.75 ± 1.00	0.83 ± 0.25
		*0.71***	*0.86****	
HFVA:Chl *a* (10^5 virus ng^{-1})	1.56 ± 0.47	5.28 ± 1.90	5.87 ± 4.22	2.23 ± 1.39
				*0.76**
Peak A (10^{-3} RU)	6.9 ± 0.3	6.0 ± 0.2	7.9 ± 0.2	8.2 ± 0.5
				*0.84***
Peak M (10^{-3} RU)	3.5 ± 0.2	2.8 ± 0.1	4.0 ± 0.2	4.1 ± 0.2
				*0.88***
Peak C (10^{-3} RU)	3.6 ± 0.2	3.1 ± 0.2	4.9 ± 0.2	4.5 ± 0.1
Peak F (10^{-3} RU)	3.3 ± 0.1	2.8 ± 0.2	5.5 ± 0.2	4.3 ± 0.1
Peak Td (10^{-3} RU)	4.4 ± 0.7	3.6 ± 0.6	6.7 ± 1.6	9.1 ± 3.1
				*0.92****
Peak Tp (10^{-3} RU)	17.2 ± 2.7	4.3 ± 1.1	8.3 ± 3.7	32.4 ± 8.8
			*−0.65**	*−0.87***

phytoplankton demise and associated prokaryotic growth. WA, on the other hand, showed an increasing abundance of high fluorescence viruses (HFVA) (Sotomayor-Garcia et al., 2020), coupled with a marked decrease in Chl *a*. This covariation between the abundance of viruses of eukaryotes and the concentration of Chl *a*, together with nutrient-replete conditions, low Herbiv index values and HPA:Chl *a* ratios (Table 1), point to viruses as the most probable cause of phytoplankton demise in WA. Phosphate concentrations increased significantly in both NSG and WA sites (Table 1), which could be indicative of the breakage of phytoplankton cells by either grazing or viral lysis, as this nutrient is easily solubilized and, therefore, detected in dissolved form upon the breakup of phytoplankton cells (Burkhardt et al., 2014).

3.2. Fluorescent organic matter (FOM)

3.2.1. FOM fractionation

Filtration of samples for fluorescent organic matter characterization had contrasting effects depending on the peak examined. Fluorescence of filtered aliquots (FDOM) was extremely similar to that of unfiltered aliquots (total FOM) for the visible peaks A, C, M and F (Fig. 1a–d). For these peaks, total FOM and FDOM showed very good linear relationships approaching the 1:1 (all slopes > 0.9 and $R^2 > 0.9$) and passing close to the 0:0 intercept. This provides confidence on our filtration procedure and suggests that suspended particles and phytoplankton cells emit very little visible fluorescence if anything. A completely different pattern was observed for the protein-like fluorescence peak T (Fig. 1e). In this case, FDOM was generally much lower than total FOM with a slope below 0.1 and a poor linear fit ($R^2 = 0.25$). Filtration of samples caused a mean reduction of peak T fluorescence of 62.2 ± 18.2 % (range 16.7–89.9 %). These results imply (i) that particles (including phytoplankton cells) excluded by filtration did contain materials with fluorescence properties similar to those of proteins, (ii) that most protein-like materials were usually found in the particulate fraction, and (iii) that the dissolved and particulate fractions of the protein-like fluorescence did not follow a simple linear relationship.

Given the good correspondence between the fluorescence of visible peaks (peaks A, C, M and F) in filtered and unfiltered aliquots, consistent

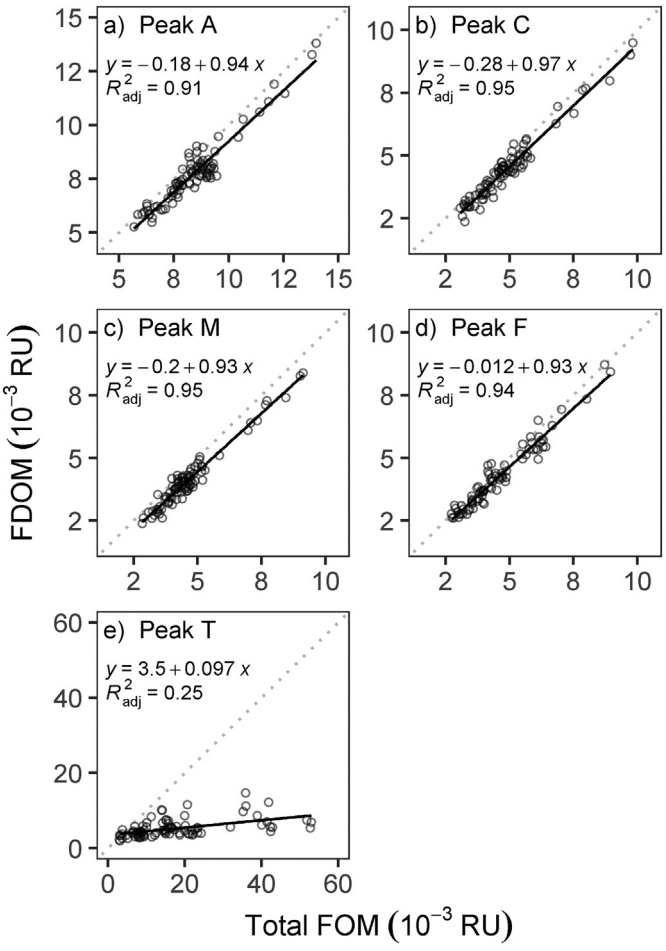

Fig. 1. Scatterplots showing OM fluorescence of filtered aliquots (FDOM) plotted against that of unfiltered counterparts (total FOM) for the five wavelength pairs examined: Peak A (a), Peak C (b), Peak M (c), Peak F (d) and Peak T (e). In each panel, the dotted line indicates the 1:1 relationship, while the solid lines are the best fit linear regression (accompanied by equation and determination coefficient). Data from all available depths is included (4–200 m).

with previous studies (Chen, 1999; Shigemitsu et al., 2020), hereinafter only the fluorescence of the filtered aliquots is considered when referring to visible peaks. For the protein-like peak T, however, we considered the fluorescence of the filtered aliquots (peak Td) and, additionally, we calculated the apparent particulate peak T fluorescence of each sample (peak Tp) as the difference in fluorescence between their filtered and unfiltered aliquots.

3.2.2. FOM composition

Fluorescent organic matter composition in the four regions visited exhibited some common patterns. Among the visible peaks examined, peak A was the dominant across all sites, with values approximately two times higher than those of peak M, in accordance with multiple studies that report peak A as the dominant visible fluorescence signal in open ocean waters (Jørgensen et al., 2011; Nelson and Gauglitz, 2016; D'Sa et al., 2021). Peak C had consistently higher fluorescence values than those of peak M. Peak F, with excitation and emission wavelengths in the higher range of the C-region (Coble, 2007), showed particularly high values in the NSG site, while in the rest (SSO, NSO and WA) it remained below the intensities of peak C. Dissolved protein-like fluorescence (peak Td) was much more variable within each region than the visible FDOM peaks, especially in the sites with higher Td fluorescence (NSG and WA). Regardless of site, particulate protein-like fluorescence (peak Tp) consistently exceeded the intensity of the dissolved protein-like peak (peak Td). Significant temporal trends were observed in two sites for various peaks: decreases in fluorescence were observed for peak Tp in NSG and WA, while increases in fluorescence throughout the visit were only detected in WA for peak A, peak M and especially for peak Td (Table 1).

3.3. Relationship of FOM composition with biotic and environmental variables

In order to identify the main drivers of the observed FOM composition, we performed a principal component analysis (PCA) based on the log-transformed biological and environmental variables that explained most of the variance of each of the FOM composition parameters examined (see methods). Supplementary ratios were projected afterwards on the already computed PCA and do not influence the ordination. Detailed results for each of the PCA active variables and projected supplementary ratios can be found in Supplementary Table 4.

The resulting PCA (Fig. 2) discriminated between the four sites visited and its two first principal components, PC1 and PC2, explained 65 % and 18.1 % of the variability, respectively. SSO occupied the negative extreme of the PC1 gradient, characterized by high SRD and Ddx:LHC, while NSG and WA were located at the opposite side of PC1, with the highest FDOM values (peaks A, M, C, S and Td), high temperatures and elevated values of the main biotic variables (Chl *a*, HPA, HFVA, LFVA and diatoms). Thus, PC1 can be viewed as a trade-off between acclimation to solar irradiance and the productivity of the system. The gradient shown by PC2, by contrast, was related to the relative abundances of autotrophs and heterotrophs. Its major positive loadings were related to specific phytoplankton groups, such as cryptophytes (Crypto) and chlorophytes (Chloro), as well as to particulate protein-like fluorescence (Tp). The main negative loadings of PC2 were variables related to the abundance of heterotrophic organisms, such as the grazing pressure (Herbiv) and the abundance of heterotrophic prokaryotes (HPA). The four sites visited were further separated by PC2, with SSO and NSG showing negative values and NSO and WA having more positive values in this axis. Overall, the projection of supplementary ratios in the PCA space (blue dashed arrows) agreed with the interpretation

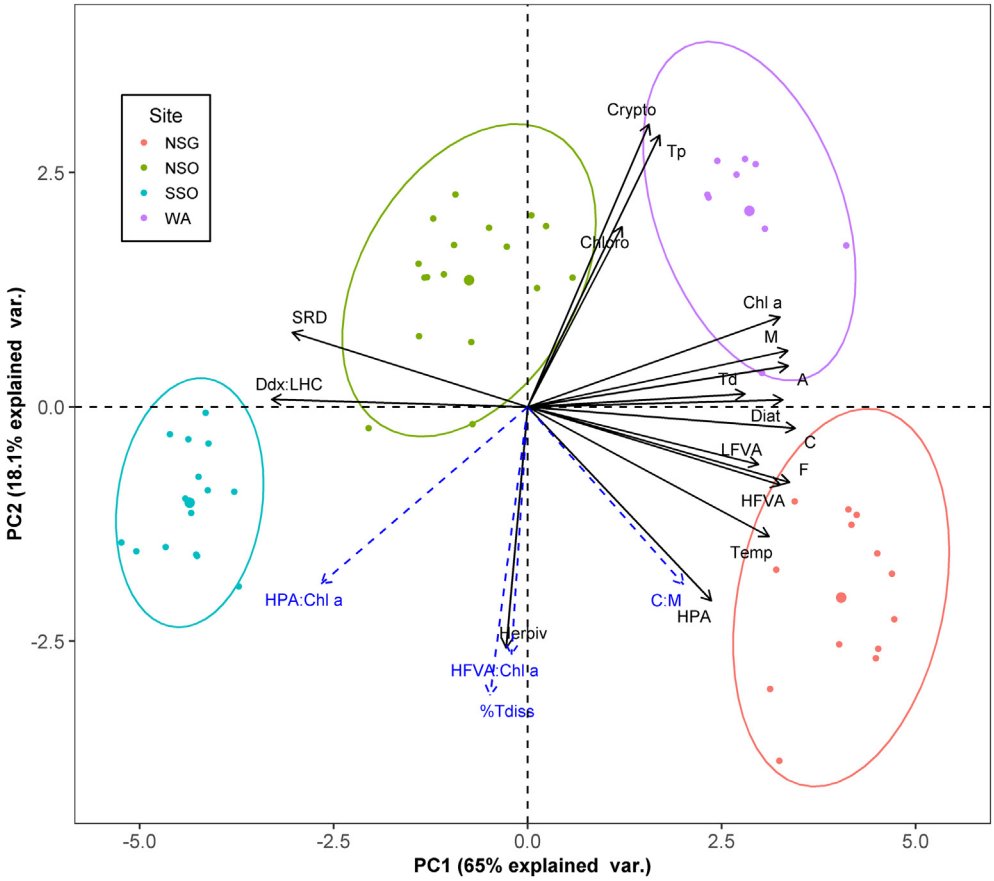

Fig. 2. Principal component analysis (PCA) of highest explanatory parameters of FOM composition in surface samples (see text). The percentage of explained variance is given on each principal component axis. Position of samples from each site are represented by small site-coloured points, and the larger points are each site centroids. Abbreviations: Diat (contribution of diatoms), Chloro (contribution of chlorophytes), Crypto (contribution of cryptophytes). Supplementary ratios (not used for the PCA calculation) are projected as blue dashed arrows.

of PC2. The HFVA:Chl *a* and HPA:Chl *a* ratios, indicative of viral pressure over phytoplankton and of the balance between consumption and production of organic matter, respectively, were negatively related to PC2. The C:M visible fluorescence ratio and the proportion total protein-like FOM found in dissolved form (%Tdiss) were also negatively correlated to PC2, suggesting their potential association with heterotrophic activities (Fig. 2).

3.4. Controls of visible fluorescent dissolved organic matter (FDOM)

Along the PC1 gradient, the visible-fluorescence peaks (A, M, C and F) occupied the opposite extreme of solar radiation dose (SRD) and phytoplankton Ddx:LHC photoprotective index (Fig. 2), which we hypothesize to be an indication of fluorescence photobleaching under high solar irradiation. Although their loadings on PC2 were lower (Supplementary Table 4), the separation of the four visible peaks along the PC2 axis might be related to differential production and/or consumption of these substances by phytoplankton and heterotrophic prokaryotes, which showed positive and negative loadings for PC2, respectively (Fig. 2). In the following sections, we explore the potential effects of photobleaching and biological activities over the FDOM visible-fluorescence composition.

3.4.1. Photobleaching of visible FDOM

The four sites visited presented a wide range of solar radiation doses (Table 1), which translated into phytoplankton communities that were affected differently by light stress, as revealed by the strong correlation between SRD and the photoprotective index Ddx:LHC ($R = 0.78$, $p < 0.001$). SSO was the site where phytoplankton communities were most affected by solar stress, followed by NSO, WA and NSG. Our results indicate that the incident solar radiation strongly influenced FDOM composition, especially in regard to the visible fluorescence (Fig. 2). We found that the combined visible fluorescence (the sum of intensities of peaks A, M, C and F) showed a strong negative correlation with SRD (R-0.82, $p < 0.001$). This correlation was even stronger with Ddx:LHC ($R = -0.90$, $p < 0.001$, Fig. 3), indicating that this photoprotective index describes the in-situ effects of solar radiation over FDOM composition better than the SRD.

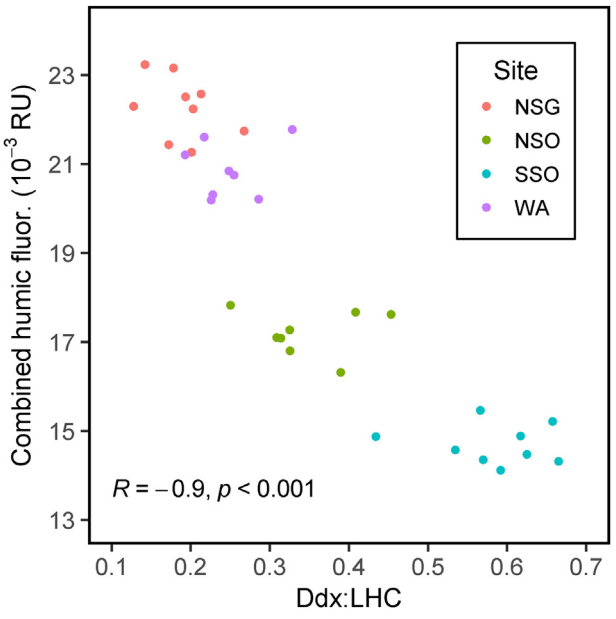

Fig. 3. Scatterplot showing the negative correlation between the surface combined humic fluorescence (sum of intensities of peaks A, M,C and F) and the photoprotective index Ddx:LHC [the ratio of diadinoxanthin (Ddx) to light harvesting carotenoids (LHC)], which quantifies the photoacclimation of phytoplankton to solar radiation (see methods). Correlation is depicted as Pearson's correlation coefficient (R). Data from surface (4 m) samples.

The photoacclimation response of phytoplankton (Ddx:LHC) depends on the light intensity that their cells are subject to, which, in turn, is controlled by the light attenuation profile and by their position in the water column (Lewis et al., 1984; Brunet et al., 2011). Phytoplankton and DOM vertical distributions in the water column are controlled by both stratification and turbulent-induced mixing (Estrada and Berdalet, 1997; Hansell et al., 2009). However, the calculation of SRD (see methods) disregards turbulent mixing and assumes that all water is effectively mixed within the mixed layer, which is defined by the position and strength of the pycnocline. Thus, discrepancies might arise between the calculated SRD and the actual irradiance that reaches phytoplankton cells and dissolved organic matter. Additionally, a 24 h integration time (SRD) might be too short to adequately reflect the cumulative impacts of irradiance on FDOM. Although the exact time integration of the Ddx:LHC ratio is difficult to assess, the observation of minor diel variations (see Fig. S6 of Nunes et al., 2019) suggests that this ratio would integrate the light history experienced by phytoplankton cells over >24 h. Consequently, the photoprotective index Ddx:LHC might be a better predictor of the "effective" solar radiation influence over FDOM composition, which helps to explain the good correlation between these parameters observed in this study (Fig. 3).

When assessed individually, every visible-fluorescence peak examined maintained the strong negative correlation with Ddx:LHC observed for the combined visible fluorescence signal. However, the shape of the inverse relationship between visible fluorescence (normalized to the maximum of each peak, see methods) and the photoprotective index was dependent on the excitation wavelength of the visible peaks (Supplementary Fig. 4). The decreasing trend of normalized fluorescence with increasing light stress (Ddx:LHC) for the shorter excitation wavelength peaks A and M (250 nm and 320 nm, respectively) were best represented by a linear function. For the longer excitation wavelength peaks C and F (340 nm and 370 nm, respectively) the relationship was best described by a logarithmic function (Table 2). Regardless of the function chosen, we observed that the longer the excitation wavelengths of the visible peaks, the more negative the slopes fitted (Table 2). This pattern suggests the existence of a gradient in relative apparent photosensitivity among the visible peaks (peak F > peak C > peak M > peak A).

This gradient of wavelength-dependent relative apparent photosensitivity of visible fluorescence is in agreement with other studies, which usually observe a blue-shift in visible fluorescence emission due to faster photobleaching at longer wavelengths (Helms et al., 2013, 2014). Moran et al. (2000), for example, observed greater loss of fluorescence for the longer excitation wavelength peak C with respect to peaks A and M when exposed to high simulated solar radiation, as well as a consistent decrease in wavelength of excitation and emission maxima for the visible fluorescence region. Working with phytoplankton exudates, Brogi et al. (2020) also found that photobleaching affected visible fluorescence differently, usually causing diminishing losses in fluorescence with decreasing excitation wavelengths of the peaks examined (emission loss: peak C > peak M > peak A). However, given that the pattern between solar radiation and visible fluorescence described above arises from correlations with field data, the slopes provided in Table 2 can only be used to rank the

Table 2
Best-fit slopes of regressions of fluorescence of visible peaks (normalized to their maximum value) with the phytoplankton photoprotective index Ddx:LHC (see methods) as predictor in surface samples. Linear model: Visible peak = a + b*Ddx:LHC; Logarithmic model: Visible peak = a + b*ln(Ddx:LHC). Highest determination coefficient for each peak is indicated in bold. All regressions were highly significant (maximum p-value = 2.36×10^{-10}).

Peak (λ_{ex})	Linear model		Logarithmic model	
	Slope	$R^2_{adj.}$	Slope	$R^2_{adj.}$
A (250 nm)	−0.53	**0.7**	−0.18	0.67
M (320 nm)	−0.67	**0.79**	−0.23	0.75
C (340 nm)	−0.78	0.76	−0.28	**0.81**
F (370 nm)	−0.93	0.67	−0.35	**0.77**

relative apparent photosensitivity of the visible fluorescence peaks, as processes other than photobleaching could be contributing to the relationships observed. Nonetheless, the good agreement between our results and those obtained in controlled photodegradation experiments point to wavelength-dependent photobleaching as the main control of the visible fluorescence composition observed in this study.

3.4.2. Biological drivers of visible FDOM

Visible fluorescence also appeared to be influenced by processes other than those related to solar radiation, as suggested by the separation of the peaks M, A, C and F along the second principal component axis (Fig. 2). Peaks M and A were related to phytoplankton-related variables (Chl *a*, Chloro, Crypto), while peaks F, C and the C:M ratio laid on the quadrant of the PCA with higher loadings of variables related to heterotrophic abundances (Herbiv, HPA, HFVA, LFVA). This distribution of peaks within the bi-dimensional space defined by PC1 and PC2 suggests that autotrophic and heterotrophic activities altered visible FDOM composition in contrasting ways.

The activity of heterotrophic prokaryotes is recognized as one of the main drivers of seawater DOM composition, as they consume, transform and release DOM of different characteristics (Carlson and Hansell, 2015). From the multiple FDOM ratios examined, a strong and highly significant positive relationship was found between the fluorescent ratio of peak C to peak M (C:M ratio) and the abundance of heterotrophic prokaryotes ($R^2 = 0.76$, $p < 0.001$, Fig. 4). This pattern is in agreement with results from previous studies on FDOM composition. Romera-Castillo et al. (2011) incubated phytoplankton exudates in the presence of prokaryotes and observed a general red shift in the emission of the visible fluorescence region, which led them to hypothesize that marine prokaryotes were preferentially utilizing blue shifted visible fluorescence substances (Peak M) and releasing red-shifted ones (Peak C). This translated into an increase in the C:M ratio as prokaryotes grew on phytoplanktonic DOM. Similar conclusions can also be drawn from field studies at the regional and global scale, which often find that apparent oxygen utilization (AOU, a proxy of the accumulated oxygen consumption by heterotrophic activity since the water body was last in contact with the atmosphere) is related to similar changes in visible fluorescence composition (De La Fuente et al., 2014). Han et al. (2021) found that the C:M ratio (derived from PARAFAC modeling) in seawater samples from the Sea of Japan increased with depth as a result of relatively higher increases in the peak C component with increasing AOU. Similarly, Catalá et al. (2016) revealed that, in the global ocean, the C-region PARAFAC component (their C1) increased with AOU much more efficiently than the M-region component (their C2), which would have led to an increased C:M ratio in the waters most affected by heterotrophic activities.

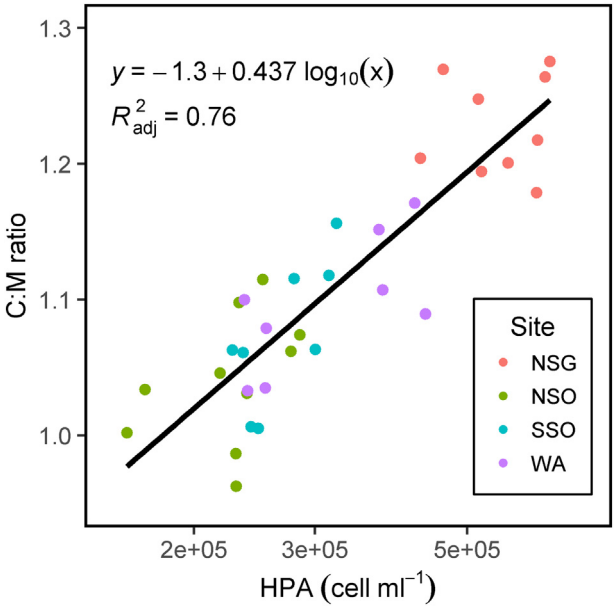

Fig. 4. Scatterplot showing the relationship between the peak C-to-peak M (C:M) fluorescence ratio and the abundance of heterotrophic prokaryotes (HPA) in surface waters. Best fit regression line, equation and coefficient of determination are also shown.

The C:M ratio, however, has also been used to infer the degree of DOM photodegradation in surface layers due to the different photolabilities of these peaks discussed earlier (Helms et al., 2013, 2014; Han et al., 2021). In our case, this ratio was indeed negatively correlated to Ddx:LHC and SRD ($R = -045$, $p = 0.0049$ and $R = -0.49$, $p = 0.0036$, respectively). We used linear model comparisons to assess the relative importance of biotic modification and photobleaching over the C:M visible fluorescence peak ratio. We found that a more complex model, taking into account both HPA and Ddx:LHC, was not significantly better at describing the variability of the C:M ratio ($p = 0.85$, F-test) than the model that considered only HPA (Fig. 4). This was expected, as the C:M ratio was in almost perfect alignment with the abundance of prokaryotes in the PCA (Fig. 2) and this ratio showed a strong loading in the PC2, poorly related to photic parameters (Ddx:LHC and SRD). Thus, our results suggest that the C:M visible fluorescence ratio was mainly driven by the activity of heterotrophic prokaryotes, whose abundances (HPA) explained 76 % of the variability of the C:M ratio.

3.5. Controls of protein-like FOM

Protein-like fluorescence exhibited marked differences from the rest of the fluorescence peaks examined in terms of filtration effects. Whereas all other wavelength pairs had similar intensities regardless of filtration, protein-like fluorescence was noticeably suppressed by filtration, implying a fractionation into particulate and dissolved FOM. In the following sections, we discuss the potential mechanisms controlling the concentration and fractionation of the protein-like fluorescence signal.

3.5.1. Particulate protein-like FOM

We hypothesize that the observed discrepancy in the protein-like fluorescence between total FOM and FDOM (Fig. 1) arises from the protein content of phytoplankton cells retained on the filter. Therefore, the apparent particulate protein fluorescence (Tp) should be related to bulk Chl *a* concentration, as marine phytoplankton cells have been reported to emit protein-like fluorescence (Determann et al., 1998; Kinsey et al., 2018). To our surprise, however, a good relationship between the particulate protein fluorescence (Tp) and Chl *a* concentration was found only when excluding the contribution of diatoms to Chl *a* concentration (Fig. 5a). When diatom-Chl *a* was included, data from the NSG site lied outside the general trend (Supplementary Fig. 5), with much less Tp than expected based on the total Chl *a* concentration. We attribute this to the high contribution of diatoms to total Chl *a* in the NSG site, which was dominated by *Eucampia antartica*, a large and heavily silicified diatom species (70 ± 10 % of NSG total phytoplankton biovolume, (Nunes et al., 2019)). Although diatoms have been reported to have lower protein contents than other phytoplankton groups (Finkel et al., 2016), this was not the case for the diatoms thriving in the NSG site, where the mean POM C:N ratio was similar to that of other sites ($p = 0.72$, Welch *t*-test). The apparent lower content of particulate protein-like fluorescence in samples with high contribution of diatoms (NSG site) would be responsible for the misalignment of Tp and Chl *a* in the PCA (Fig. 2), as diatoms were dominant in the NSG site, which also exhibited the highest Chl *a* concentrations (Table 1). Thus, Tp in the PCA was alternatively aligned with the abundances of other phytoplankton groups, such as chlorophytes and, specially, cryptophytes (Fig. 2), which were the dominant groups in the NSO and WA sites (Table 1).

We hypothesize that diatom silica frustules might be responsible for the reduced UV fluorescence at NSG. Silica frustules do not only protect diatoms against grazing (Assmy et al., 2013), viral infection (Kranzler et al., 2019) and bacterial remineralization (Moriceau et al., 2009; Cabrera-Brufau et al., 2021), they also seem to shield diatom cells from potentially

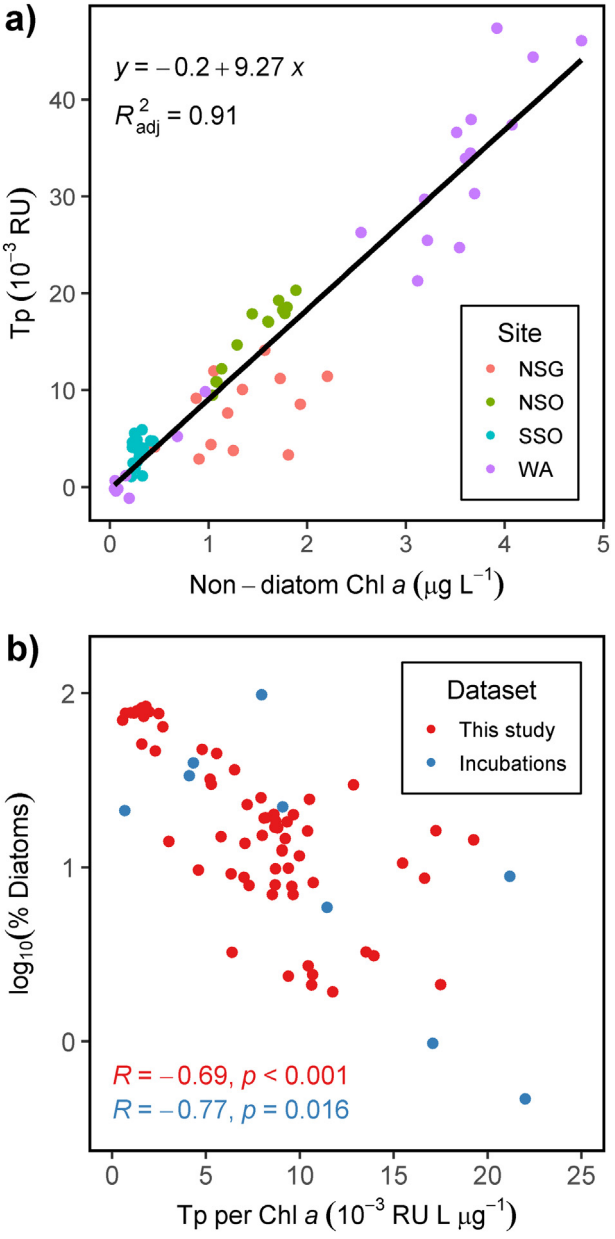

Fig. 5. Scatterplots showing the relationship between: (a) particulate protein fluorescence (Tp) and non-diatom Chl *a* concentration, and (b) proportion of diatom contribution to Chl *a* (this study, red dots) or to total phytoplankton biomass (incubations, blue dots) and particulate protein-like fluorescence (Tp) per unit of Chl *a*. Formula and solid line in panel a are the best fit linear regression. Pearson correlation coefficients and p-values are shown in panel b for data from this study (in red) and for Mediterranean incubations (in blue, see text). Data from all depths of PEGASO cruise (4-200 m) are included in both panels, additional data from Mediterranean incubations are shown in panel b (blue dots).

harmful wavelengths (Aguirre et al., 2018). The microstructure of silica frustules exhibits photonic properties that reduce the incident UV radiation via photoluminescence, absorption, re-focusing and scattering (Ghobara et al., 2019; Goessling et al., 2021). The transmittance of silica frustules is particularly low for the wavelength range used to quantify protein-like materials (~20 % at 280–315 nm range) (De Tommasi et al., 2018). This physiological adaptation might help diatoms to thrive in highly UV-irradiated environments, such as the Southern Ocean (Ellegaard et al., 2016), but it would also have actively reduced the fluorescence signal of unfiltered aliquots, locally shading diatom cells from the excitation beam (centered at 280 nm) during the protein-like fluorescence quantification. This effect would have resulted in the strong negative correlation observed between the contribution of diatoms to total Chl *a* concentration and the apparent particulate protein fluorescence per unit of Chl *a* ($R = -0.69$, $p < 0.001$, Fig. 5b). Interestingly, using data from incubations of Mediterranean phytoplankton populations, enriched with different amounts of silicate to obtain contrasting diatom dominances (Cabrera-Brufau et al., 2021), we observed a similar correlation ($R = -0.77$, $p = 0.016$, Fig. 5b) albeit with the proportion of diatoms quantified in terms of diatom contribution to total phytoplankton biomass.

The previous interpretation might help to explain the results of Cyr et al. (2017). Using on-line glider based measurements of Chl *a* and protein-like fluorescence in the NW Mediterranean, they noticed some differences in the vertical and seasonal distributions of both variables. They hypothesized that the observed mismatches could be related to seasonal changes in phytoplankton community composition (Marty et al., 2002; Nunes et al., 2018). During the spring bloom, typically dominated by diatoms, they report high Chl *a* concentrations and low protein-like fluorescence values, while in summer, when small non-diatom species predominate, they observed a protein-like fluorescence 3 times higher than in spring despite similar Chl *a* values. The lower Tp fluorescence per Chl *a* yielded by samples with high diatom contributions in our study (Fig. 5b) could help to explain these seasonal differences. However, as the study of Cyr et al. (2017) was based on in-situ (i.e. non-filtered) protein-like and Chl *a* fluorescence profiles, their results were probably influenced both by changes of in-vivo Chl *a* fluorescence efficiencies and by the dynamics of truly dissolved peak T fluorescence, which makes a direct comparison difficult.

The relationships between diatom dominance and particulate protein-like fluorescence found in our study could be influenced by processes that were not taken into account here. For example, although absorbance was used to correct fluorescence underestimations due to inner-filter effects (see methods) and quantification of Chl *a* via the use of glass fiber filters (GF/F) does account for contributions of smaller picophytoplankton (Chavez et al., 1995), the potential protein-like fluorescence of non-phytoplanktonic particles could not be quantified with the available data. Thus, although 91 % of peak Tp variability was explained by non-diatom Chl *a* alone, the proposed hypothesis should be further investigated under laboratory controlled conditions.

3.5.2. Protein-like FOM fractionation

The lack of a simple linear relationship between the protein-like fluorescence of unfiltered and filtered aliquots (Fig. 1) implies that the concentration of protein-like FDOM (Peak Td) cannot not be explained by the amount of peak Tp fluorescence alone. Although in the PCA ordination Td was aligned with the first principal component (Fig. 2), this protein-like FDOM was not well represented by this first axis, as derived by the much lower squared cosine of this peak ($\cos^2 = 0.63$) when compared to that of the rest of FDOM peaks ($\cos^2$: 0.91–0.96). This was further corroborated by the low variance of Td explained by either Chl *a* concentration (Chl *a*, $R^2 = 0.30$) or the photoprotective index (Ddx:LHC, $R^2 = 0.28$), two of the main driving variables of the PC1 (Fig. 2). The low explanatory power of the photoprotective index is in agreement with other studies, which find little effects of photobleaching on protein-like FDOM (Moran et al., 2000; Zhang et al., 2013; Brogi et al., 2020). Additionally, although phytoplankton directly produce protein-like FDOM (Romera-Castillo et al., 2010; Chari et al., 2013), Chl *a* concentration has been shown to be an unsuitable predictor of dissolved peak T variability (Jørgensen et al., 2011; Catalá et al., 2016). This suggests that processes other than photobleaching and direct phytoplankton production are influencing protein-like FDOM distributions in the ocean.

In order to better understand the mechanisms that control the fractionation of protein-like fluorescence into particulate (Tp) and dissolved form (Td), we examined the proportion of total protein-like fluorescence found in dissolved form (%Tdiss) in relation to other parameters. We found that %Tdiss was well represented by the second principal component of the PCA (Coordinate $= -0.88$, $\cos^2 = 0.77$, Supplementary Table 4), in which it was tightly aligned with the herbivory index (Herbiv) and with

the ratio of abundance of high fluorescence viruses to Chl *a* concentration (HFVA:Chl *a*) (Fig. 2). We assessed the predictive power of these two parameters over %Tdiss using linear regressions. We found that the HFVA:Chl *a* ratio was a good predictor of the proportion of dissolved peak T (R^2 = 0.65, Supplementary Fig. 6a). Although the variance in %Tdiss explained by the Herbiv index alone was relatively low (R^2 = 0.24, Supplementary Fig. 6b), the combination of these two parameters, Herbiv index and HFVA:Chl *a* ratio, was a significantly better predictor of the observed variance in %Tdiss (R^2 = 0.78, Fig. 6) than the HFVA:Chl *a* ratio alone (p = 0.0047, F-test).

We interpret these results as a consequence of the combined effects of grazers (from nanoflagellates to mesozooplankton) and viral activities over the phytoplankton populations. Grazing and viral infections lead to the rupture of phytoplankton cells and the release of the intracellular materials, transferring protein-like fluorescence from particulate (Tp) into dissolved (Td) forms and increasing %Tdiss. This interpretation is supported by the temporal dynamics of these protein-like fluorescence pools observed during the visits to the NSG and WA sites, where phytoplankton abundances were in decrease (Table 1). On average, the HFVA:Chl *a* ratio and the Herbiv index explained 51 % and 29 % of the %Tdiss variability in the multiple regression model, respectively (Fig. 6). Thus, considering all the results of this study, we conclude viral lysis was the main driver of protein-like fluorescence fractionation.

3.5.3. Case study: mode of bloom demise and fate of protein-like FOM

The sampling design allowed us to monitor the short-term temporal evolution of the chemical and biological properties of seawater at each site, following the same water mass over 1.5–3 days and identifying trends in phytoplankton bloom dynamics and OM processing. Regarding OM fluorescence, we found a common temporal trend in NSG and WA, wherein the particulate protein-like fluorescence decreased significantly during the time of visit (Fig. 7a, b). This decrease was coupled with decreases in Chl *a* concentration (Table 1) and with increases in signs of distinct phytoplankton mortality agents for each site. In WA, where the phytoplankton community was dominated by cryptophytes, we observed a strong increase in the abundance of high fluorescence viruses (HFVA) both in absolute terms and, especially, with respect to Chl *a* (R = 0.76, p < 0.05, Fig. 7b). By contrast, in NSG, where diatoms where the dominant phytoplankton group, we did not find a significant increase in the abundances of high fluorescence viruses (R = −0.17, p = 0.6), yet the zooplankton grazing, as derived from the Herbiv index, increased markedly through time (R = 0.95, p < 0.001, Fig. 7a). Additionally, the concentration of fecal pellets in NSG also increased significantly during the visit (Supplementary Table 3), presumably from copepods, which were also observed in this site through light microscopy. This apparent group-specific phytoplankton loss pattern is in agreement with Biggs et al. (2021), who found that diatoms and cryptophytes were subject to contrasting loss processes. They show that, over a full Antarctic productive season, viral lysis accounted for 63 % of the specific loss rates of cryptophyte biomass, whereas grazing represented 56 % of biomass loss in the case of diatoms. In our case, the particulate protein-like fluorescence decreased markedly in both sites, as the viral pressure on cryptophytes (in WA) and the zooplanktonic pressure on diatoms (in NSG) increased trough time, with WA and NSG losing 55 % and 47 % of their initial particulate protein-like fluorescence during the 32 and 72 h of monitoring, respectively.

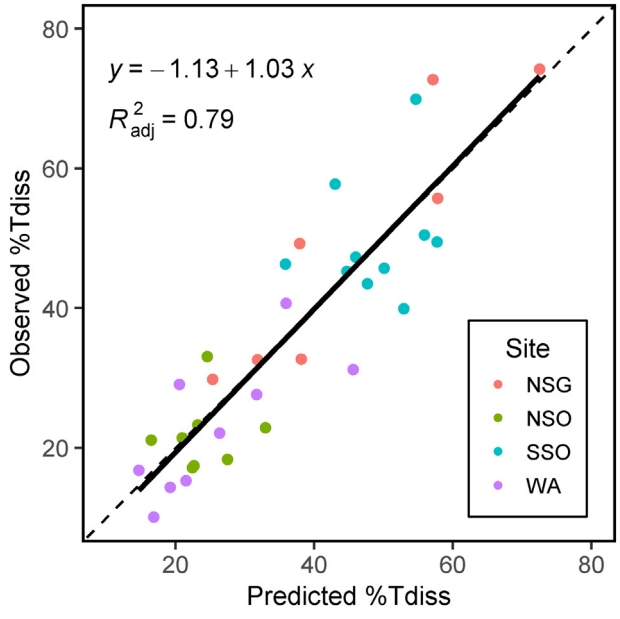

Fig. 6. Scatterplot of observed vs predicted values for proportion of peak T dissolved (%Tdiss) based on multiple linear regression with Herbiv index and HFVA:Chl *a* ratio as predictors. Multiple regression equation: %Tdiss = −209 + 60*Herbiv + 43* $\log_{10}$(HFVA:Chl *a*), multiple adjusted-R^2 = 0.78, Herbiv partial R^2 = 0.29, $\log_{10}$(HFVA:Chl *a*) partial R^2 = 0.51. The equation is the regression model for the relationship between the observed vs predicted data (solid line). The 1:1 line is also shown (dashed line).

The consequences of these two modes of phytoplankton bloom demise were very different for each site. Although we cannot discard some DOM consumption by the growing prokaryotic community at NSG (Table 1), no significant increases were detected in this site for either dissolved protein-like fluorescence (Td, Fig. 7c) or any of the other FDOM peaks examined (Table 1) as a consequence of zooplankton grazing (Fig. 7a). It seems that the loss of phytoplanktonic biomass (Chl *a*) and of particulate protein-like materials (Tp) at the NSG site were mostly channeled through ingestion by grazers and subsequent production of fecal pellets (Supplementary Table 3), with no detectable solubilization into FDOM (Table 1). In the WA site, however, the increase in viral pressure (HFVA:Chl *a*) was coupled to a synchronous accumulation of dissolved protein-like fluorescence (Td) (Fig. 7b, d) and of FDOM peaks A and M (Table 1) largely attributed to phytoplankton (Fig. 2). Overall, the relatively low explanatory power of the Herbiv index over %Tdiss variability (Fig. 6), joined with the contrasting FOM dynamics at NSG and WA sites (Fig. 7, Table 1), suggest that zooplankton grazing is not as efficient as viral infection in transferring phytoplanktonic organic matter from the particulate into the dissolved pool.

The high efficiency of zooplankton in transferring particulate protein-like substances to higher trophic levels, and the high efficiency of viral lysis in transferring them to the dissolved organic pool have important ecological and biogeochemical consequences for the cycling of organic matter in marine systems. The role of zooplankton and viruses in controlling phytoplankton populations and the demise of blooms is well-known in marine ecology (Brussaard, 2004; Steinberg and Landry, 2017). Their biological activities not only reduce the standing stock of phytoplankton, but channel a significant fraction of the phytoplanktonic OM into distinct ecological and biogeochemical pathways. Although zooplankton can contribute to the dissolved organic matter pool through excretion and sloppy feeding (Lampert, 1978; Møller, 2007), they primarily contribute to transfer of C to larger metazoans and to C export through the production of fast-sinking fecal pellets (Steinberg and Landry, 2017), which often dominate C export fluxes in the Southern Ocean (Gleiber et al., 2012). Viral infections, on the other hand, although can also lead to enhanced C export by promoting aggregation and sinking of infected cells (Zimmerman et al., 2020), channel most phytoplankton C away from higher trophic levels by releasing it as DOM, a process named the “viral shunt” (Fuhrman, 1999; Suttle, 2007; Jover et al., 2014). Thus, the termination of phytoplankton blooms caused by viruses favors the recycling of organic matter near the surface through the microbial loop (Bratbak et al., 1994; Biggs et al., 2021), as lysis makes phytoplanktonic biomass accessible to heterotrophic prokaryotes in the form of DOM, effectively lowering the trophic level at which phytoplankton biomass enters the trophic web.

Protein-like fluorescent DOM is usually considered to be bioavailable, with multiple studies reporting fast consumption of these DOM fluorescence signals by heterotrophic prokaryotes, either directly determined during dark incubations (Lønborg et al., 2010, 2015) or inferred from protein-

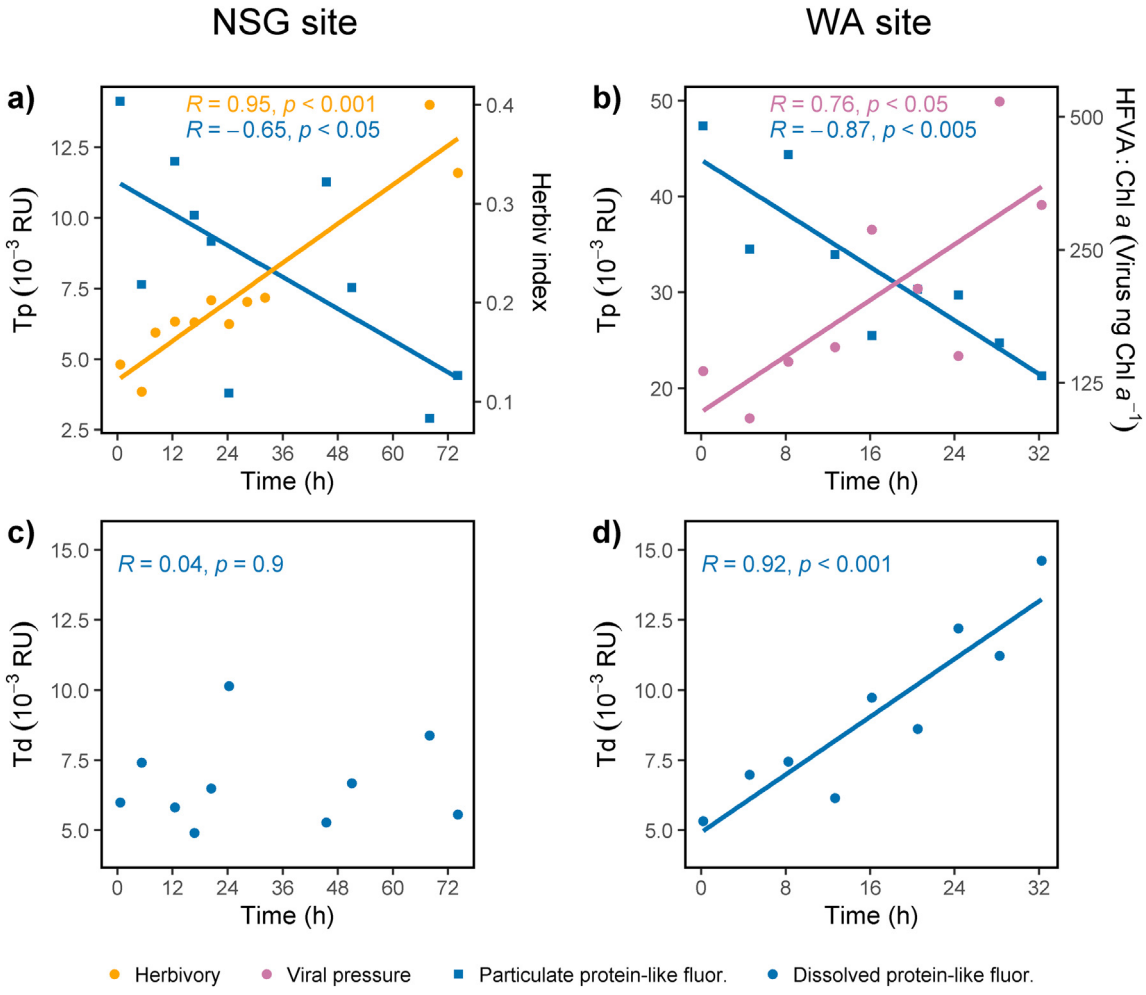

Fig. 7. Scatterplots showing the temporal evolution of the various chemical and biological parameters in surface waters of NSG (panels a, c) and WA (panels b, c) sites analyzed in this study. The top panels depict the temporal evolution of particulate protein-like fluorescence (Tp, blue squares) and of the herbivory index (Herbiv, orange dots) in NSG (a) and the HFVA:Chl *a* ratio (purple dots) in WA (b). The lower panels show the temporal evolution of dissolved protein-like fluorescence (Td, blue dots) in NSG (c) and in the WA site (d). In each panel we show the temporal correlation of each parameter (as Pearson coefficients) and, only for significant temporal correlations ($p < 0.05$), the best-fit regression line is added.

like FDOM distribution in the water column (Misic et al., 2006; Nelson and Gauglitz, 2016). Peak Td fluorescence can be used as an indication of the concentration of total amino acids (Yamashita and Tanoue, 2003), which are, along with dissolved proteins, preferred substrates for bacteria in Antarctic marine waters (Simon and Rosenstock, 2007; Simon et al., 2012). The efficient solubilization of protein-like fluorescence in WA was therefore expected to promote the growth of heterotrophic prokaryotes. However, we were not able to detect any increases in the abundances of heterotrophic prokaryotes during our visit to WA ($R = 0.17$, $p = 0.75$). Top-down control of prokaryotes by bacteriophages (Vaqué et al., 2017) or ciliates (Duarte et al., 2005) was unlikely, as there were no differences in the bacteriophage-to-prokaryote ratio (LFVA:HPA) between the NSG and the WA site ($p = 0.52$, Student *t*-test) and the ciliate-to-prokaryote ratio was higher in NSG ($p < 0.001$, Welch t-test), where prokaryotic growth was observed (Table 1). Thus, the lack of detection of prokaryotic growth in WA was most probably because the sampling duration at this site (32 h) was shorter than the three to four days time-lag typically observed for Antarctic prokaryotes to begin to growth upon substrate additions (Massana et al., 2001; Dyda et al., 2009; Simon et al., 2012).

4. Summary and conclusions

The fluorescent organic matter composition encountered in the surface waters of four Southern Ocean sites reflects how this organic matter pool is strongly influenced by both environmental conditions and biological activities. Our study reinforces the potential of combining single excitation-emission fluorescence measurements to gain valuable insights into the distribution, dynamics, and drivers of fluorescent organic matter in the ocean.

The comparison between the organic matter fluorescence measured in filtered and unfiltered aliquots has shown that the filtration procedure has little effect on visible fluorescence intensities, allowing comparisons between online fluorescence sensors and discrete laboratory measurements of filtered samples. Protein-like fluorescence, however, was strongly affected by filtration, with phytoplankton cells being responsible for a large but variable proportion of the total protein-like fluorescence in unfiltered aliquots. Thus, we recommend caution when interpreting protein-like fluorescence distributions obtained from unfiltered samples and in-situ sensors, as those results could be not directly comparable to studies examining true dissolved organic matter fluorescence, especially in highly productive regions. In addition, although further experimental studies are required, the apparently lower specific protein-like fluorescence of diatoms could serve as a fast and inexpensive way of approximating the dominance of this group in the phytoplankton community.

Regarding the drivers of FDOM composition identified in surface waters, we found that visible fluorescence was mainly controlled by radiation-induced photobleaching, with the several peaks examined exhibiting contrasting apparent photolabilities positively related to their excitation wavelengths. Despite the indirect nature of the measurement,

we found that phytoplankton photoacclimation was a better predictor of visible fluorescence photobleaching than the calculated solar radiation dose. Finally, the taxonomic composition of the phytoplankton communities encountered did not have a straightforward effect on FDOM composition. Instead, the stage of phytoplankton bloom development seemed to be the main biotic control over the organic matter fluorescence composition. In our study, visible FDOM composition was related to the abundance of heterotrophic prokaryotes even under strong solar irradiance conditions. Protein-like fluorescence, on the other hand, was mainly controlled by biotic processes of phytoplankton mortality, with viral and, to a lesser extent, zooplanktonic pressure over phytoplankton populations accurately predicting the proportion of protein-like fluorescence found in the dissolved pool.

Overall, this study contributes to better understanding the sources and drivers of fluorescent organic matter in Antarctic waters. In particular, the novel insights into the fractionation of the protein-like fluorescent organic matter pool reported here might help to disentangle the complex dynamics governing the coupling of primary producers with prokaryotic recyclers via the supply of bioavailable dissolved organic matter in the marine system.

CRediT authorship contribution statement

MC-B, CM, PC and RS designed the study. MC-B processed the data and wrote the manuscript with the assistance of CM and PC. MMS and RS obtained funding. RS led the cruise. CM, EO-R, SN, ME, MMS, DV, GLP and RS analyzed samples and provided data. All authors revised, corrected and approved the final manuscript.

Declaration of competing interest

The authors declare that they have no known competing financial interests or personal relationships that could have appeared to influence the work reported in this paper.

Acknowledgments

The study was funded by the Spanish Government through projects PEGASO (CTM2012-37615), BIOGAPS (CTM2016-81008-R) and DOGMA (PID2020-112653GB-I00). MC-B was supported by a predoctoral fellowship from the Spanish Government (FPU16/01925). We thank the captain and crew of the BIO Hespérides and the Unidad de Tecnología Marina (UTM-CSIC) for their valuable help during the cruise. We are grateful to the researchers and technicians who participated in the cruise, analyzed samples and pre-processed ancillary data (C. Antequera, V. Balagué, E. Borrull, C. Cardelús, P. Cortés, M. Dall'Osto, M. Delgado, A. Duró, M. Emelianov, I. Ferrera, D. López, M. Mestre, P. Rodríguez-Ros, S.J. Royer and M. Zamanillo). We thank M. Abad at the Nutrient Analysis Service of the ICM-CSIC for nutrient analysis. We also acknowledge the institutional support of the "Severo Ochoa Centre of Excellence" accreditation (CEX2019-000928-S) from the Spanish government. This study is part of the POLARCSIC platform activities.

Appendix A. Supplementary data

Supplementary data to this article can be found online at https://doi.org/10.1016/j.scitotenv.2022.156921.

References

Abdi, H., Williams, L.J., 2010. Principal component analysis. Wiley Interdiscip. Rev. Comput. Stat. 2 (4), 433–459. https://doi.org/10.1002/wics.101.

Aguirre, L.E., Ouyang, L., Elfwing, A., Hedblom, M., Wulff, A., Inganäs, O., 2018. Diatom frustules protect DNA from ultraviolet light. Sci. Rep. 8 (1), 1–6. https://doi.org/10.1038/s41598-018-21810-2.

Alderkamp, A.C., Mills, M.M., Dijken, V.G.L., Arrigo, K.R., 2013. Photoacclimation and non-photochemical quenching under in situ irradiance in natural phytoplankton assemblages from the Amundsen Sea, Antarctica. Mar. Ecol. Prog. Ser. 475, 15–34. https://doi.org/10.3354/meps10097.

Assmy, P., Smetacek, V., Montresor, M., Klaas, C., Henjes, J., Strass, V.H., Arrieta, J.M., Bathmann, U., Berg, G.M., Breitbarth, E., Cisewski, B., Friedrichs, L., Fuchs, N., Herndl, G.J., Jansen, S., Krägefsky, S., Latasa, M., Peeken, I., Röttgers, R., Scharek, R., Schüller, S.E., Steigenberger, S., Webb, A., Wolf-Gladrow, D., 2013. Thick-shelled, grazer-protected diatoms decouple ocean carbon and silicon cycles in the iron-limited Antarctic circumpolar current. Proc. Natl. Acad. Sci. U. S. A. 110 (51), 20633–20638. https://doi.org/10.1073/pnas.1309345110.

Azam, F., Fenchel, T., Field, J., Gray, J., Meyer-Reil, L., Thingstad, F., 1983. The ecological role of water-column microbes in the sea. Mar. Ecol. Prog. Ser. 10, 257–263. https://doi.org/10.3354/meps010257.

Biggs, T.E.G., Huisman, J., Brussaard, C.P.D., 2021. Viral lysis modifies seasonal phytoplankton dynamics and carbon flow in the Southern Ocean. ISME J., 1–8. https://doi.org/10.1038/s41396-021-01033-6 May.

Bratbak, G., Thingstad, F., Heldal, M., 1994. Viruses and the microbial loop. Microb. Ecol. 28 (2), 209–221. https://doi.org/10.1007/BF00166811.

Brogi, S.R., Charrière, B., Gonnelli, M., Vaultier, F., Sempéré, R., Vestri, S., Santinelli, C., 2020. Effect of uv and visible radiation on optical properties of chromophoric dissolved organic matter released by emiliania huxleyi. J. Mar. Sci. Eng. 8 (11), 1–15. https://doi.org/10.3390/jmse8110888.

Brunet, C., Johnsen, G., Lavaud, J., Roy, S., 2011. In: Pigments, In Phytoplankton, Roy, S., Llewellyn, C., Egeland, E.S., Johnsen, G. (Eds.), Pigments and Photoacclimation Processes. Cambridge University Press, Cambridge, pp. 445–471. https://doi.org/10.1017/CBO9780511732263.017.

Brussaard, C.P.D., 2004. Viral control of phytoplankton populations-a Review1. J. Eukaryot. Microbiol. 51 (2), 125–138. https://doi.org/10.1111/j.1550-7408.2004.tb00537.x.

Brussaard, C.P.D., Payet, J.P., Winter, C., Weinbauer, M.G., 2010. Quantification of aquatic viruses by flow cytometry. Man. Aquat. Viral Ecol. 2004, 102–109. https://doi.org/10.4319/mave.2010.978-0-9845591-0-7.102.

Brym, A., Paerl, H.W., Montgomery, M.T., Handsel, L.T., Ziervogel, K., Osburn, C.L., 2014. Optical and chemical characterization of base-extracted particulate organic matter in coastal marine environments. Mar. Chem. 162, 96–113. https://doi.org/10.1016/j.marchem.2014.03.006 Elsevier B.V.

Burkhardt, B.G., Watkins-Brandt, K.S., Defforey, D., Paytan, A., White, A.E., 2014. Remineralization of phytoplankton-derived organic matter by natural populations of heterotrophic bacteria. Mar. Chem. 163, 1–9. https://doi.org/10.1016/j.marchem.2014.03.007 Elsevier B.V.

Cabrera-Brufau, M., Arin, L., Sala, M.M., Cermeño, P., Marrasé, C., 2021. Diatom dominance enhances resistance of phytoplanktonic POM to mesopelagic microbial decomposition. Front. Mar. Sci. 8. https://doi.org/10.3389/fmars.2021.683354.

Cao, F., Zhu, Y., Kieber, D.J., Miller, W.L., 2020. Distribution and photo-reactivity of chromophoric and fluorescent dissolved organic matter in the Northeastern North Pacific Ocean. Deep Sea Res. Part I Oceanogr. Res. Pap. 155 (June 2019), 103168. https://doi.org/10.1016/j.dsr.2019.103168. Elsevier Ltd.

Carlson, C.A., Hansell, D.A., 2015. DOM sources, sinks, reactivity, and budgets. In Biogeochemistry of Marine Dissolved Organic Matter: Second Edition, Second edi., 65–126 https://doi.org/10.1016/B978-0-12-405940-5.00003-0.

Carstea, E.M., Popa, C.L., Baker, A., Bridgeman, J., 2020. In situ fluorescence measurements of dissolved organic matter: a review. Sci. Total Environ. 699, 134361. https://doi.org/10.1016/j.scitotenv.2019.134361.

Catalá, T.S., Álvarez-Salgado, X.A., Otero, J., Iuculano, F., Companys, B., Horstkotte, B., Romera-Castillo, C., Nieto-Cid, M., Latasa, M., Morán, X.A.G., Gasol, J.M., Marrasé, C., Stedmon, C.A., Reche, I., 2016. Drivers of fluorescent dissolved organic matter in the global epipelagic ocean. Limnol. Oceanogr. 61 (3), 1101–1119. https://doi.org/10.1002/lno.10281.

Cefarelli, A.O., Vernet, M., Ferrario, M.E., 2011. Phytoplankton composition and abundance in relation to free-floating Antarctic icebergs. Deep. Res. Part II Top. Stud. Oceanogr. 58 (11–12), 1436–1450. https://doi.org/10.1016/j.dsr2.2010.11.023.

Chari, N.V.H.K., Keerthi, S., Sarma, N.S., Pandi, S.R., Chiranjeevulu, G., Kiran, R., Koduru, U., 2013. Fluorescence and absorption characteristics of dissolved organic matter excreted by phytoplankton species of western Bay of Bengal under axenic laboratory condition. J. Exp. Mar. Bio. Ecol. 445, 148–155. https://doi.org/10.1016/j.jembe.2013.03.015 Elsevier B.V.

Chavez, F.P., Buck, K.R., Bidigare, R.R., Karl, D.M., Hebel, D., Latasa, M., Campbell, L., Newton, J., 1995. On the chlorophyll a retention properties of glass-fiber GF/F filters. Limnol. Oceanogr. 40 (2), 428–433. https://doi.org/10.4319/lo.1995.40.2.0428.

Cheah, W., Soppa, M.A., Wiegmann, S., Ossebaar, S., Laglera, L.M., Strass, V.H., Santos-Echeandía, J., Hoppema, M., Wolf-Gladrow, D., Bracher, A., 2017. Importance of deep mixing and silicic acid in regulating phytoplankton biomass and community in the iron-limited Antarctic polar front region in summer. Deep Sea resPart II Top. Stud. Oceanogr. 138, 74–85. https://doi.org/10.1016/j.dsr2.2016.05.019.

Chen, R.F., 1999. In situ fluorescence measurements in coastal waters. Org. Geochem. 30 (6), 397–409. https://doi.org/10.1016/S0146-6380(99)00025-X.

Chen, M., Jung, J., Lee, Y.K., Kim, T.W., Hur, J., 2019. Production of tyrosine-like fluorescence and labile chromophoric dissolved organic matter (DOM)and low surface accumulation of low molecular weight-dominated DOM in a productive Antarctic se. Mar. Chem. 213 (April), 40–48. https://doi.org/10.1016/j.marchem.2019.04.009 Elsevier.

Coble, P.G., 1996. Characterization of marine and terrestrial DOM in seawater using excitation-emission matrix spectroscopy. Mar. Chem. 51 (4), 325–346. https://doi.org/10.1016/0304-4203(95)00062-3.

Coble, P.G., 2007. Marine optical biogeochemistry: the chemistry of ocean color. Chem. Rev. 107 (2), 402–418. https://doi.org/10.1021/cr050350.

Cory, R.M., McKnight, D.M., 2005. Fluorescence spectroscopy reveals ubiquitous presence of oxidized and reduced quinones in dissolved organic matter. Environ. Sci. Technol. 39 (21), 8142–8149. https://doi.org/10.1021/es0506962.

Costa, R.R., Mendes, C.R.B., Tavano, V.M., Dotto, T.S., Kerr, R., Monteiro, T., Odebrecht, C., Secchi, E.R., 2020. Dynamics of an intense diatom bloom in the northern Antarctic peninsula, february 2016. Limnol. Oceanogr. 65 (9), 2056–2075. https://doi.org/10.1002/lno.11437.

Cyr, F., Tedetti, M., Besson, F., Beguery, L., Doglioli, A.M., Petrenko, A.A., Goutx, M., 2017. A new glider-compatible optical sensor for dissolved organic matter measurements: test case from the NW Mediterranean Sea. Front. Mar. Sci. 4 (MAR), 1–19. https://doi.org/10.3389/fmars.2017.00089.

Dainard, P.G., Guéguen, C., McDonald, N., Williams, W.J., 2015. Photobleaching of fluorescent dissolved organic matter in Beaufort Sea and North Atlantic Subtropical Gyre. Mar. Chem. 177, 630–637. https://doi.org/10.1016/j.marchem.2015.10.004. Elsevier B.V.

De La Fuente, P., Marrasé, C., Canepa, A., Antón Álvarez-Salgado, X., Gasser, M., Fajar, N.M., Romera-Castillo, C., Pelegrí, J.L., 2014. Does a general relationship exist between fluorescent dissolved organic matter and microbial respiration?-The case of the dark equatorial Atlantic Ocean. Deep. Res. Part I Oceanogr. Res. Pap. 89 (May 2010), 44–55. https://doi.org/10.1016/j.dsr.2014.03.007 Elsevier.

De Tommasi, E., Congestri, R., Dardano, P., De Luca, A.C., Managò, S., Rea, I., De Stefano, M., 2018. UV-shielding and wavelength conversion by centric diatom nanopatterned frustules. Sci. Rep. 8 (1), 1–14. https://doi.org/10.1038/s41598-018-34651-w.

Determann, S., Lobbes, J.örg M., Reuter, R., Rullkötter, J.ürgen, 1998. Ultraviolet fluorescence excitation and emission spectroscopy of marine algae and bacteria. Mar. Chem. 62 (1–2), 137–156. https://doi.org/10.1016/S0304-4203(98)00026-7.

D'Sa, E.J., Kim, H.C., 2017. Surface gradients in dissolved organic matter absorption and fluorescence properties along the New Zealand sector of the southern ocean. Front. Mar. Sci. 4 (FEB), 1–14. https://doi.org/10.3389/fmars.2017.00021.

D'Sa, E.J., Kim, H.-C., Ha, S.-Y., Joshi, I., 2021. Ross Sea dissolved organic matter optical properties during an austral summer: biophysical influences. Front. Mar. Sci. 8 (October), 1–18. https://doi.org/10.3389/fmars.2021.749096.

Duarte, C.M., Agustí, S., Vaqué, D., Agawin, N.S.R., Felipe, J., Casamayor, E.O., Gasol, J.M., 2005. Experimental test of bacteria-phytoplankton coupling in the Southern Ocean. Limnol. Oceanogr. 50 (6), 1844–1854. https://doi.org/10.4319/lo.2005.50.6.1844.

Dyda, R.Y., Suzuki, M.T., Yoshinaga, M.Y., Rodger Harvey, H., 2009. The response of microbial communities to diverse organic matter sources in the Arctic Ocean. Deep. Res. Part II Top. Stud. Oceanogr. 56 (17), 1249–1263. https://doi.org/10.1016/j.dsr2.2008.10.019.

Ellegaard, M., Lenau, T., Lundholm, N., Maibohm, C., Friis, S.M.M., Rottwitt, K., Su, Y., 2016. The fascinating diatom frustule—can it play a role for attenuation of UV radiation? J. Appl. Phycol. 28 (6), 3295–3306. https://doi.org/10.1007/s10811-016-0893-5.

Elser, J.J., Bracken, M.E.S., Cleland, E.E., Gruner, D.S., Harpole, W.S., Hillebrand, H., Ngai, J.T., Seabloom, E.W., Shurin, J.B., Smith, J.E., 2007. Global analysis of nitrogen and phosphorus limitation of primary producers in freshwater, marine and terrestrial ecosystems. Ecol. Lett. 10 (12), 1135–1142. https://doi.org/10.1111/j.1461-0248.2007.01113.x.

Estrada, M., Berdalet, E., 1997. Phytoplankton in a turbulent world. Sci. Mar. 61 (SUPPL.1), 125–140.

Evans, C., Pearce, I., Brussaard, C.P.D., 2009. Viral-mediated lysis of microbes and carbon release in the sub-Antarctic and polar frontal zones of the australian Southern Ocean. Environ. Microbiol. 11 (11), 2924–2934. https://doi.org/10.1111/j.1462-2920.2009.02050.x.

Field, C.B., Behrenfeld, M.J., Randerson, J.T., Falkowski, P., 1998. Primary production of the biosphere: integrating terrestrial and oceanic components. Science 281 (5374), 237–240. https://doi.org/10.1126/science.281.5374.237.

Finkel, Z.V., Follows, M.J., Liefer, J.D., Brown, C.M., Benner, I., Irwin, A.J., 2016. Phylogenetic diversity in the macromolecular composition of microalgae. PLoS One 11 (5), 1–16. https://doi.org/10.1371/journal.pone.0155977.

Fortier, L., Le Fèvre, J., Legendre, L., 1994. Export of biogenic carbon to fish and to the deep ocean: the role of large planktonic microphages. J. Plankton Res. 16 (7), 809–839. https://doi.org/10.1093/plankt/16.7.809.

Fuhrman, J.A., 1999. Marine viruses and their biogeochemical and ecological effects. Nature 399 (6736), 541–548. https://doi.org/10.1038/21119.

Fukuzaki, K., Imai, I., Fukushima, K., Ishii, K.I., Sawayama, S., Yoshioka, T., 2014. Fluorescent characteristics of dissolved organic matter produced by bloom-forming coastal phytoplankton. J. Plankton Res. 36 (3), 685–694. https://doi.org/10.1093/plankt/fbu015.

Gasol, J.M., Del Giorgio, P.A., 2000. Using flow cytometry for counting natural planktonic bacteria and understanding the structure of planktonic bacterial communities. Sci. Mar. 64 (2), 197–224. https://doi.org/10.3989/scimar.2000.64n2197.

Ghobara, M.M., Ghobara, M.M., Mazumder, N., Vinayak, V., Reissig, L., Gebeshuber, I.C., Tiffany, M.A., Gordon, R., Gordon, R., 2019. On light and diatoms: a photonics and photobiology review. In: Seckbach, J., Gordon, R. (Eds.), Diatoms: Fundamentals and Applications, pp. 129–189. https://doi.org/10.1002/9781119370741.ch7 Wiley.

Gleiber, M.R., Steinberg, D.K., Ducklow, H.W., 2012. Time series of vertical flux of zooplankton fecal pellets on the continental shelf of the western Antarctic peninsula. Mar. Ecol. Prog. Ser. 471, 23–36.

Goessling, J.W., Yanyan, S., Kühl, M., Ellegaard, M., 2021. Frustule photonics and light harvesting strategies in diatoms. In: Annenkov, V., Seckback, J., Gordon, R. (Eds.), Diatom Morphogenesis, pp. 269–300. https://doi.org/10.1002/9781119488170.ch12 Wiley.

Methods of seawater analysis. In: Grasshoff, K., Kremling, K., Ehrhardt, M. (Eds.), Marine Chemistry, Third edit. https://doi.org/10.1016/0304-4203(78)90045-2 John Wiley & Sons.

Han, H., Cho, H.M., Kwon, H.K., Kim, G., 2021. Fluorescent dissolved organic matter (FDOM) in the East Sea (Japan Sea): distributions, sources, and sinks. Ocean Sci. J. 56 (2), 132–140. https://doi.org/10.1007/s12601-021-00014-2. Korea Institute of Ocean Science & Technology and The Korean Society of Oceanography.

Hansell, D.A., Carlson, C.A., Repeta, D.J., Schlitzer, R., 2009. Dissolved organic matter in the ocean a controversy stimulates new insights. Oceanography 22 (SPL.ISS. 4), 202–211. https://doi.org/10.5670/oceanog.2009.109.

Helms, J.R., Stubbins, A., Perdue, E.M., Green, N.W., Chen, H., Mopper, K., 2013. Photochemical bleaching of oceanic dissolved organic matter and its effect on absorption spectral slope and fluorescence. Mar. Chem. 155, 81–91. https://doi.org/10.1016/j.marchem.2013.05.015 Elsevier B.V.

Helms, J.R., Mao, J., Stubbins, A., Schmidt-Rohr, K., Spencer, R.G.M., Hernes, P.J., Mopper, K., 2014. Loss of optical and molecular indicators of terrigenous dissolved organic matter during long-term photobleaching. Aquat. Sci. 76 (3), 353–373. https://doi.org/10.1007/s00027-014-0340-0.

Higgins, H.W., Wright, S.W., Schlüter, L., 2011. In: Pigments, In Phytoplankton, Roy, S., Llewellyn, C., Egeland, E.S., Johnsen, G. (Eds.), Quantitative Interpretation of Chemotaxonomic Pigment Data. Cambridge University Press, Cambridge, pp. 257–313. https://doi.org/10.1017/CBO9780511732263.010.

Hillebrand, H., Dürselen, C.-D., Kirschtel, D., Pollingher, U., Zohary, T., 1999. Biovolume calculation for pelagic and benthic microalgae. J. Phycol. 35 (2), 403–424. https://doi.org/10.1046/j.1529-8817.1999.3520403.x.

Jørgensen, L., Stedmon, C.A., Kragh, T., Markager, S., Middelboe, M., Søndergaard, M., 2011. Global trends in the fluorescence characteristics and distribution of marine dissolved organic matter. Mar. Chem. 126 (1–4), 139–148. https://doi.org/10.1016/j.marchem.2011.05.002 Elsevier B.V.

Jover, L.F., Effler, T.C., Buchan, A., Wilhelm, S.W., Weitz, J.S., 2014. The elemental composition of virus particles: implications for marine biogeochemical cycles. Nat. Rev. Microbiol. 12 (7), 519–528. https://doi.org/10.1038/nrmicro3289. Nature Publishing Group.

Kinsey, J.D., Corradino, G., Ziervogel, K., Schnetzer, A., Osburn, C.L., 2018. Formation of chromophoric dissolved organic matter by bacterial degradation of phytoplankton-derived aggregates. Front. Mar. Sci. 4 (JAN), 1–16. https://doi.org/10.3389/fmars.2017.00430.

Kothawala, D.N., Murphy, K.R., Stedmon, C.A., Weyhenmeyer, G.A., Tranvik, L.J., 2013. Inner filter correction of dissolved organic matter fluorescence. Limnol. Oceanogr. Methods 11 (DEC), 616–630. https://doi.org/10.4319/lom.2013.11.616.

Kranzler, C.F., Krause, J.W., Brzezinski, M.A., Edwards, B.R., Biggs, W.P., Maniscalco, M., McCrow, J.P., Van Mooy, B.A.S., Bidle, K.D., Allen, A.E., Thamatrakoln, K., 2019. Silicon limitation facilitates virus infection and mortality of marine diatoms. Nat. Microbiol. 4 (11), 1790–1797. https://doi.org/10.1038/s41564-019-0502-x Springer US.

Kraus, T.E.C., Anderson, C.A., Morgenstern, K., Downing, B.D., Pellerin, B.A., Bergamaschi, B.A., 2010. Determining sources of dissolved organic carbon and disinfection byproduct precursors to the McKenzie River. Oregon. J. Environ. Qual. 39 (6), 2100–2112. https://doi.org/10.2134/jeq2010.0030.

Kropuenske, L.R., Mills, M.M., van Dijken, G.L., Bailey, S., Robinson, D.H., Welschmeyer, N.A., Arrigoa, K.R., 2009. Photophysiology in two major Southern Ocean phytoplankton taxa: photoprotection in Phaeocystis Antarctica and Fragilariopsis cylindrus. Limnol. Oceanogr. 54 (4), 1176–1196. https://doi.org/10.4319/lo.2009.54.4.1176.

Lampert, W., 1978. Release of dissolved organic carbon by grazing zooplankton. Limnol. Oceanogr. 23 (4), 831–834. https://doi.org/10.4319/lo.1978.23.4.0831.

Landry, M.R., Selph, K.E., Brown, S.L., Abbott, M.R., Measures, C.I., Vink, S., Allen, C.B., Calbet, A., Christensen, S., Nolla, H., 2002. Seasonal dynamics of phytoplankton in the Antarctic polar front region at 170°W. Deep. Res. Part II topStud. Oceanogr. 49 (9–10), 1843–1865. https://doi.org/10.1016/S0967-0645(02)00015-2.

Latasa, M., 2014. A simple method to increase sensitivity for RP-HPLC phytoplankton pigment analysis. Limnol. Oceanogr. Methods 12 (1 JAN), 46–53. https://doi.org/10.4319/lom.2014.12.46.

Lawaetz, A.J., Stedmon, C.A., 2009. Fluorescence intensity calibration using the Raman scatter peak of water. Appl. Spectrosc. 63 (8), 936–940. https://doi.org/10.1366/000370209788964548.

Legendre, L., 1990. The significance of microalgal blooms for fisheries and for the export of particulate organic carbon in oceans. J. Plankton Res. 12 (4), 681–699. https://doi.org/10.1093/plankt/12.4.681.

Levitus, S., 1982. Climatological Atlas of the World Ocean. US Department of Commerce, National Oceanic and Atmospheric Administration.

Lewis, M., Cullen, J., Piatt, T., 1984. Relationships between vertical mixing and photoadaptation of phytoplankton: similarity criteria. Mar. Ecol. Prog. Ser. 15, 141–149. https://doi.org/10.3354/meps015141.

Lønborg, C., Álvarez-Salgado, X.A., Davidson, K., Martínez-García, S., Teira, E., 2010. Assessing the microbial bioavailability and degradation rate constants of dissolved organic matter by fluorescence spectroscopy in the coastal upwelling system of the Ría de Vigo. Mar. Chem. 119 (1–4), 121–129. https://doi.org/10.1016/j.marchem.2010.02.001 Elsevier B.V.

Lønborg, C., Yokokawa, T., Herndl, G.J., Antón Álvarez-Salgado, X., 2015. Production and degradation of fluorescent dissolved organic matter in surface waters of the eastern north Atlantic ocean. Deep. Res. Part I Oceanogr. Res. Pap. 96, 28–37. https://doi.org/10.1016/j.dsr.2014.11.001 Elsevier.

Marañón, E., Cermeño, P., Fernández, E., Rodríguez, J., Zabala, L., 2004. Significance and mechanisms of photosynthetic production of dissolved organic carbon in a coastal eutrophic ecosystem. Limnol. Oceanogr. 49 (5), 1652–1666. https://doi.org/10.4319/lo.2004.49.5.1652.

Martínez-Pérez, A.M., Nieto-Cid, M., Osterholz, H., Catalá, T.S., Reche, I., Dittmar, T., Álvarez-Salgado, X.A., 2017. Linking optical and molecular signatures of dissolved organic matter in the Mediterranean Sea. Sci. Rep. 7 (1), 1–11. https://doi.org/10.1038/s41598-017-03735-4.

Marty, J.C., Chiavérini, J., Pizay, M.D., Avril, B., 2002. Seasonal and interannual dynamics of nutrients and phytoplankton pigments in the western Mediterranean Sea at the DYFAMED time-series station (1991-1999). Deep. Res. Part II Top. Stud. Oceanogr. 49 (11), 1965–1985. https://doi.org/10.1016/S0967-0645(02)00022-X.

Massana, R., Pedrós-Alió, C., Casamayor, E.O., Gasol, J.M., 2001. Changes in marine bacterioplankton phylogenetic composition during incubations designed to measure

biogeochemically significant parameters. Limnol. Oceanogr. 46 (5), 1181–1188. https://doi.org/10.4319/lo.2001.46.5.1181.
Mendes, C.R.B., de Souza, M.S., Garcia, V.M.T., Leal, M.C., Brotas, V., Garcia, C.A.E., 2012. Dynamics of phytoplankton communities during late summer around the tip of the Antarctic peninsula. Deep Sea resPart I Oceanogr. Res. Pap. 65, 1–14. https://doi.org/10.1016/j.dsr.2012.03.002.
Mendes, C.R.B., Kerr, R., Tavano, V.M., Cavalheiro, F.A., Garcia, C.A.E., Gauns Dessai, D.R., Anilkumar, N., 2015. Cross-front phytoplankton pigments and chemotaxonomic groups in the Indian sector of the Southern Ocean. Deep. Res. Part II Top. Stud. Oceanogr. 118, 221–232. https://doi.org/10.1016/j.dsr2.2015.01.003 Elsevier.
Misic, C., Castellano, M., Ruggieri, N., Povero, P., 2006. Dissolved organic matter characterisation and temporal trends in Terra Nova Bay (Ross Sea, Antarctica). Estuar. Coast. Shelf Sci. 70 (3), 405–414. https://doi.org/10.1016/j.ecss.2006.06.024.
Moline, M.A., 1998. Photoadaptive response during the development of a coustal Antarctic diatom bloom and relationship to water column stability. Limnol. Oceanogr. 43 (1), 146–153 Wiley Online Library.
Møller, E.F., 2007. Production of dissolved organic carbon by sloppy feeding in the copepods Acartia tonsa, Centropages typicus, and Temora longicornis. Limnol. Oceanogr. 52 (1), 79–84. https://doi.org/10.4319/lo.2007.52.1.0079.
Moore, C., Barnard, A., Fietzek, P., Lewis, M.R., Sosik, H.M., White, S., Zielinski, O., 2009. Optical tools for ocean monitoring and research. Ocean Sci. 5 (4), 661–684. https://doi.org/10.5194/os-5-661-2009.
Mopper, K., Kieber, D.J., Stubbins, A., 2015. Marine photochemistry of organic matter: processes and impacts. processes and impacts. Biogeochemistry of Marine Dissolved Organic Matter: Second Edition, Second Edi. Elsevier Inc. https://doi.org/10.1016/B978-0-12-405940-5.00008-X.
Moran, M.A., Sheldon, W.M., Zepp, R.G., 2000. Carbon loss and optical property changes during long-term photochemical and biological degradation of estuarine dissolved organic matter. Limnol. Oceanogr. 45 (6), 1254–1264. https://doi.org/10.4319/lo.2000.45.6.1254.
Moriceau, B., Goutx, M., Guigue, C., Lee, C., Armstrong, R., Duflos, M., Tamburini, C., Charrière, B., Ragueneau, O., 2009. Si-C interactions during degradation of the diatom skeletonema marinoi. Deep. Res. Part II Top. Stud. Oceanogr. 56 (18), 1381–1395. https://doi.org/10.1016/j.dsr2.2008.11.026.
Murphy, K.R., Stedmon, C.A., Waite, T.D., Ruiz, G.M., 2008. Distinguishing between terrestrial and autochthonous organic matter sources in marine environments using fluorescence spectroscopy. Mar. Chem. 108 (1–2), 40–58. https://doi.org/10.1016/j.marchem.2007.10.003.
Nelson, N.B., Gauglitz, J.M., 2016. Optical signatures of dissolved organic matter transformation in the global ocean. Front. Mar. Sci. 2 (JAN), 1–15. https://doi.org/10.3389/fmars.2015.00118.
Nunes, S., Latasa, M., Gasol, J.M., Estrada, M., 2018. Seasonal and interannual variability of phytoplankton community structure in a Mediterranean coastal site. Mar. Ecol. Prog. Ser. 592, 57–75. https://doi.org/10.3354/meps12493.
Nunes, S., Latasa, M., Delgado, M., Emelianov, M., Simó, R., Estrada, M., 2019. Phytoplankton community structure in contrasting ecosystems of the Southern Ocean: South Georgia, South Orkneys and western Antarctic Peninsula. Deep. Res. Part I Oceanogr. Res. Pap. 151 (May), 103059. https://doi.org/10.1016/j.dsr.2019.06.005 Elsevier Ltd.
Para, J., Coble, P.G., Charrière, B., Tedetti, M., Fontana, C., Sempéré, R., 2010. Fluorescence and absorption properties of chromophoric dissolved organic matter (CDOM) in coastal surface waters of the northwestern Mediterranean Sea, influence of the Rhône River. Biogeosciences 7 (12), 4083–4103. https://doi.org/10.5194/bg-7-4083-2010.
Romera-Castillo, C., Sarmento, H., Álvarez-Salgado, X.A., Gasol, J.M., Marrasé, C., 2010. Production of chromophoric dissolved organic matter by marine phytoplankton. Limnol. Oceanogr. 55 (1), 446–454. https://doi.org/10.4319/lo.2010.55.1.0446.
Romera-Castillo, C., Sarmento, H., Alvarez-Salgado, X.A.Á., Gasol, J.M., Marrasé, C., 2011. Net production and consumption of fluorescent colored dissolved organic matter by natural bacterial assemblages growing on marine phytoplankton exudates. Appl. Environ. Microbiol. 77 (21), 7490–7498. https://doi.org/10.1128/AEM.00200-11.
Shigemitsu, M., Uchida, H., Yokokawa, T., Arulananthan, K., Murata, A., 2020. Determining the distribution of fluorescent organic matter in the Indian Ocean using in situ fluorometry. Front. Microbiol. 11 (December), 1–15. https://doi.org/10.3389/fmicb.2020.589262.
Simon, M., Rosenstock, B., 2007. Different coupling of dissolved amino acid, protein, and carbohydrate turnover to heterotrophic picoplankton production in the Southern Ocean in austral summer and fall. Limnol. Oceanogr. 52 (1), 85–95. https://doi.org/10.4319/lo.2007.52.1.0085.
Simon, M., Billerbeck, S., Kessler, D., Selje, N., Schlingloff, A., 2012. Bacterioplankton communities in the Southern Ocean: composition and growth response to various substrate regimes. Aquat. Microb. Ecol. 68 (1), 13–28. https://doi.org/10.3354/ame01597.
Sotomayor-Garcia, A., Sala, M.M., Ferrera, I., Estrada, M., Vázquez-Domínguez, E., Emelianov, M., Cortés, P., Marrasé, C., Ortega-Retuerta, E., Nunes, S., Castillo, Y.M., Cuerva, M.S., Sebastián, M., Dall'osto, M., Simó, R., Vaqué, D., 2020. Assessing viral abundance and community composition in four contrasting regions of the Southern Ocean. Life 10 (7), 1–20. https://doi.org/10.3390/life10070107.
Stedmon, C.A., Nelson, N.B., 2015. The optical properties of DOM in the ocean. Biogeochemistry of Marine Dissolved Organic Matter: Second Edition, Second Edi Elsevier Inc. https://doi.org/10.1016/B978-0-12-405940-5.00010-8.
Steinberg, D.K., Landry, M.R., 2017. Zooplankton and the ocean carbon cycle. Annu. Rev. Mar. Sci. 9 (1), 413–444. https://doi.org/10.1146/annurev-marine-010814-015924.
Sullivan, C.W., Arrigo, K.R., McClain, C.R., Comiso, J.C., Firestone, J., 1993. Distributions of phytoplankton blooms in the Southern Ocean. Science 262 (5141), 1832–1837. https://doi.org/10.1126/science.262.5141.1832.
Suttle, C.A., 2007. Marine viruses - major players in the global ecosystem. Nat. Rev. Microbiol. 5 (10), 801–812. https://doi.org/10.1038/nrmicro1750.
Taylor, M.H., Losch, M., Bracher, A., 2013. On the drivers of phytoplankton blooms in the Antarctic marginal ice zone: a modeling approach. J. Geophys. Res. Ocean. 118 (1), 63–75. https://doi.org/10.1029/2012JC008418.
Utermöhl, H., 1958. Zur Vervollkommnung der quantitativen Phytoplankton-Methodik. 1953–1996SIL Commun. 9 (1), 1–38. https://doi.org/10.1080/05384680.1958.11904091. Taylor & Francis.
Vallina, S.M., Simó, R., 2007. Strong relationship between DMS and the solar radiation dose over the global surface ocean. Science 315 (5811), 506–508. https://doi.org/10.1126/science.1133680.
Vaqué, D., Boras, J.A., Torrent-Llagostera, F., Agustí, S., Arrieta, J.M., Lara, E., Castillo, Y.M., Duarte, C.M., Sala, M.M., 2017. Viruses and protists induced-mortality of prokaryotes around the Antarctic peninsula during the austral summer. Front. Microbiol. 8 (MAR), 1–12. https://doi.org/10.3389/fmicb.2017.00241.
Wedborg, M., Persson, T., Larsson, T., 2007. On the distribution of UV-blue fluorescent organic matter in the Southern Ocean. Deep. Res. Part I Oceanogr. Res. Pap. 54 (11), 1957–1971. https://doi.org/10.1016/j.dsr.2007.07.003.
Yamashita, Y., Tanoue, E., 2003. Chemical characterization of protein-like fluorophores in DOM in relation to aromatic amino acids. Mar. Chem. 82 (3–4), 255–271. https://doi.org/10.1016/S0304-4203(03)00073-2.
Yamashita, Y., Panton, A., Mahaffey, C., Jaffé, R., 2011. Assessing the spatial and temporal variability of dissolved organic matter in Liverpool Bay using excitation-emission matrix fluorescence and parallel factor analysis. Ocean Dyn. 61 (5), 569–579. https://doi.org/10.1007/s10236-010-0365-4.
Yentsch, C.S., Menzel, D.W., 1963. A method for the determination of phytoplankton chlorophyll and phaeophytin by fluorescence. Deep Sea Res. Oceanogr. Abstr. 10 (3), 221–231. https://doi.org/10.1016/0011-7471(63)90358-9.
Zamanillo, M., Ortega-Retuerta, E., Nunes, S., Estrada, M., Sala, M.M., Royer, S.J., López-Sandoval, D.C., Emelianov, M., Vaqué, D., Marrasé, C., Simó, R., 2019. Distribution of transparent exopolymer particles (TEP) in distinct regions of the Southern Ocean. Sci. Total Environ. 691, 736–748. https://doi.org/10.1016/j.scitotenv.2019.06.524. Elsevier B.V.
Zhang, Y., Liu, X., Osburn, C.L., Wang, M., Qin, B., Zhou, Y., 2013. Photobleaching response of different sources of chromophoric dissolved organic matter exposed to natural solar radiation using absorption and excitation-emission matrix spectra. PLoS One 8 (10). https://doi.org/10.1371/journal.pone.0077515.
Zhang, C., Dang, H., Azam, F., Benner, R., Legendre, L., Passow, U., Polimene, L., Robinson, C., Suttle, C.A., Jiao, N., 2018. Evolving paradigms in biological carbon cycling in the ocean. Natl. Sci. Rev. 5 (4), 481–499. https://doi.org/10.1093/nsr/nwy074.
Zimmerman, A.E., Howard-Varona, C., Needham, D.M., John, S.G., Worden, A.Z., Sullivan, M.B., Waldbauer, J.R., Coleman, M.L., 2020. Metabolic and biogeochemical consequences of viral infection in aquatic ecosystems. Nat. Rev. Microbiol. 18 (1), 21–34. https://doi.org/10.1038/s41579-019-0270-x Springer US.